LAWRENCE
LIVERMORE
NATIONAL
LABORATORY

LLNL-JRNL-805508

Metatsable-solid phase diagrams derived from polymorphic solidification kinetics

B. Sadigh, L. Zepeda-Ruiz, J. Belof

February 21, 2020

Proceedings of National Academy of Sciences

Disclaimer

Metastable–solid phase diagrams derived from polymorphic solidification kinetics

Babak Sadigh[a,1], Luis Zepeda-Ruiz[a], and Jonathan L. Belof[a,1]

[a]Lawrence Livermore National Laboratory, Physical and Life Sciences Directorate, Livermore, CA 94550

Edited by Pablo G. Debenedetti, Princeton University, Princeton, NJ, and approved January 16, 2021 (received for review August 24, 2020)

Nonequilibrium processes during solidification can lead to kinetic stabilization of metastable crystal phases. A general framework for predicting the solidification conditions that lead to metastable-phase growth is developed and applied to a model face-centered cubic (fcc) metal that undergoes phase transitions to the body-centered cubic (bcc) as well as the hexagonal close-packed phases at high temperatures and pressures. Large-scale molecular dynamics simulations of ultrarapid freezing show that bcc nucleates and grows well outside of the region of its thermodynamic stability. An extensive study of crystal–liquid equilibria confirms that at any given pressure, there is a multitude of metastable solid phases that can coexist with the liquid phase. We define for every crystal phase, a solid cluster in liquid (SCL) basin, which contains all solid clusters of that phase coexisting with the liquid. A rigorous methodology is developed that allows for practical calculations of nucleation rates into arbitrary SCL basins from the undercooled melt. It is demonstrated that at large undercoolings, phase selections made during the nucleation stage can be undone by kinetic instabilities amid the growth stage. On these bases, a solidification–kinetic phase diagram is drawn for the model fcc system that delimits the conditions for macroscopic grains of metastable bcc phase to grow from the melt. We conclude with a study of unconventional interfacial kinetics at special interfaces, which can bring about heterogeneous multiphase crystal growth. A first-order interfacial phase transformation accompanied by a growth-mode transition is examined.

phase transitions | kinetic stabilization | metastability | solidification | phase diagram

The idea of polymorphism of solid nuclei during crystallization dates back to Ostwald (1). It results from a lack of explicit correlation between the bulk free energies of different crystal phases and their respective interfacial free energies with the liquid. It is thus expected that the early stages of nucleation are likely to be dominated by the crystal phase with the smallest solid–melt interfacial free energy and the later stages by the equilibrium bulk phase (2). It has been recognized that classical nucleation theory (CNT) and density-functional theory (3), as well as phase-field models (4), need to be generalized to account for structural phase transformations of the growing nuclei as the ratio of the interface to the bulk regions changes. This so-called two-step nucleation has been observed experimentally in rapidly quenched metals (5), as well as block copolymer solutions (6, 7) and charged colloidal particles (8, 9), where metastable body-centered cubic (bcc) phase clusters are reported to occur before final crystallization into the face-centered cubic (fcc) phase takes place. A more dramatic outcome at large undercooling is that of nucleation of metastable solid phases that can under suitable circumstances, grow to macroscopic sizes. A large body of literature has grown over the past several decades in which rapid solidification of mainly metals and alloys, at cooling rates on the order of 10^4 to 10^5 K, has been studied in containerless experiments through electromagnetic/electrostatic levitation techniques (10–14), where strong undercooling is achieved by avoiding heterogenous nucleation. Through X-ray diffraction of the freely suspended droplets, the dynamics of crystal nucleation during solidification have been investigated. As a result, solidification of diverse crystalline phases such as fcc, bcc, icosahedral, and quasicrystalline has been observed, and emergence of metastable phases, often in the bcc structure, in sufficiently undercooled liquids has been demonstrated. Through application of CNT, the undercooling necessary for metastable-phase growth has been rationalized. It is conjectured that phase selection takes place in the nucleation stage; the phase emerging is one with the smallest critical nucleation barrier. Consequently, models for solid–liquid interfacial free energies of different crystal phases have been derived from these experiments. Nevertheless, controversies remain when nucleation of metastable phases cannot be explained based on their interfacial free energies. Instead, the likely culprit is suspected to be preferential nucleation at the droplet surfaces (13).

Recent powerful advances in dynamic shock/ramp compression techniques (15–23) have been able to achieve melting and solidification at rates that can exceed rapid cooling techniques described above. Hence, extreme undercoolings can be achieved in these experiments, and therefore, the limits of the current theories of phase transformation kinetics can be tested. These laboratory experiments are currently at the forefront of unraveling fundamental insights into the kinetics of solidification at extreme conditions. Freezing under such conditions is believed

Significance

Kinetic stabilization of metastable phases in rapidly cooled metals and alloys has been established in experiments for decades. However, atomistic theories that can quantitatively predict the solidification conditions that produce nonequilibrium phases are still in their infancy. Recent advances in pulsed power/laser technologies, as well as in situ characterization, have brought to bear unprecedented understanding of matter at extreme temperatures and pressures. However, accurate predictions of kinetic stabilization of metastable phases that are necessary for physical interpretation of these experiments are lacking. This work provides a blueprint for development of kinetic phase maps of materials undergoing rapid solidification from first principles. Through atomistic simulations, the phases dominating nucleation are identified, and their kinetic stabilities during the growth stage are characterized.

Author contributions: B.S., L.Z.-R., and J.L.B. designed research; B.S. and L.Z.-R. performed research; B.S. and L.Z.-R. analyzed data; and B.S. and J.L.B. wrote the paper.

The authors declare no competing interest.

This article is a PNAS Direct Submission.

[1]To whom correspondence may be addressed. Email: sadigh1@llnl.gov or belof1@llnl.gov.

This article contains supporting information online at https://www.pnas.org/lookup/suppl/doi:10.1073/pnas.2017809118/-/DCSupplemental.

Published February 22, 2021.

to play a major role in determining the structure of the planetary cores, which in turn, is responsible for many important properties (e.g., whether a planet can support a magnetic dynamo). It is thus essential to develop capabilities for predicting metastable-phase formation under these nonequilibrium conditions.

From a theoretical standpoint, the preference for nucleation of the bcc and the icosahedral phases from the undercooled liquid was first predicted decades ago through Landau expansion in density fluctuations near the liquid phase (24). The observation of two-step nucleation in molecular dynamics (MD) simulations was initially inconclusive (25–28). The majority of attempts failed to demonstrate any convincing signature of intermediate phases during nucleation. The breakthrough came through the work of ten Wolde et al. (29, 30), where they performed umbrella sampling (31) simulations using the bond-orientational order parameter Q_6 (32, 33) to induce crystallization at moderate undercoolings. They thus observed nucleation of predominantly bcc crystallites that would transform to fcc in their cores while the interface regions remained bcc. This finding was later reproduced by classical density-functional theory (34). Subsequently, it was observed that when varying both pressure and undercooling, one could make the bcc precritical crystallites grow to large sizes (35, 36).

In the following, we derive from atomistic first principles the kinetic maps of the crystal phases that are stabilized by nonequilibrium processes during solidification. For this purpose, we generalize the CNT and challenge the assumption that the precritical nucleation stage is solely responsible for crystal phase selection during freezing. Hence, rather than studying the intricacies of multistage nucleation and its effects on the rate of solidification (37–40), we focus on the product phases that result from liquid–solid transformation kinetics and derive kinetic phase boundaries. The latter specifies the undercooling conditions, in the neighborhood of which multiple crystal phases are likely to grow from the melt. Near these boundaries, the postcritical stage can play a big role in promoting or impeding the growth of competing crystal phases. Hence, in contrast to thermodynamic phase boundaries that are straightforward consequences of thermodynamic rules that can never be violated given enough time, kinetic phase maps are mere guidelines for high-probability events and depend on the particular experimental context being considered. Nevertheless, metastable-phase maps are crucial for understanding solidification near the triple points of the thermodynamic phase diagram, where the liquid phase coexists with two solid phases.

CNT describes solidification in the language of canonical transition-state theory. It uses as the reaction coordinate the size of the solid cluster that nucleates inside the melt. It relies on separation of timescales involving two distinct processes: activation of critical nuclei and growth of postcritical solid clusters. The critical nucleus is the transition state that separates the liquid and the solid basins of attraction. The rate of solid-phase nucleation is dictated by the flux of trajectories through the critical nucleus. It is assumed that the solid-phase nuclei grow slowly enough that they can be considered near equilibrium at all times. A consequence of this is that the sizes of the critical nuclei can be put in one to one correspondence with the undercooling temperature. Furthermore, solid clusters can be stabilized within the melt by constraining volume and energy fluctuations through change of statistical ensemble, from open (e.g., isothermal–isobaric) to closed (e.g., microcanonical). This has been successfully utilized in computer simulations and has allowed the study of equilibrium shapes and sizes of solid clusters in liquid, as well as their coexistence temperatures (41). Through the Gibbs–Thomson (GT) condition, this information has been used to extract solid–liquid interfacial free energies under the assumption of negligible anisotropy (41–43). Later in this paper, we will formulate a rigorous foundation for this approach and as a result, present a general algorithm for conveniently calculating accurate interfacial free energies that incorporate interfacial anisotropy as well as finite cluster-size curvature effects.

Let us now examine the phase space of the undercooled liquid by carving it into distinct subspaces, each containing all of the configurations of solid clusters of a particular phase ϕ, coexisting with the liquid phase. We refer to each such region as the ϕ-SCL (solid cluster in liquid) basin. The relative rates of nucleation of solids belonging to two different basins ϕ_1 and ϕ_2 are proportional to $\exp(-\Delta G/k_B T)$, where ΔG is the Gibbs free energy difference between the critical nuclei of the two phases at the undercooling temperature T. ΔG has contributions from free energies of both the bulk solids as well as the solid–liquid interfaces. Hence, it is easy to see that at large-enough undercooling, when the critical nuclei are relatively small, the interfacial free energy may favor nucleation of the phase that is not the thermodynamically stable bulk phase. However, during the growth stage, the thermodynamic driving force for transformation to the thermodynamic equilibrium phase increases. It is thus imperative to identify under what conditions the thus nucleated metastable-phase clusters can grow to form micrometer-sized grains without transforming to the thermodynamically stable phase. For this purpose, we define the metastable solid cluster in liquid (MSCL) subspace, which is the collection of microstates that are weakly connected to other SCL basins. More precisely, nuclei that belong to the MSCL subspace do not undergo solid–solid transformations during their growth stage, which for a micrometer-sized grain and a typical interface velocity of 10 m/s, is on the submicrosecond timescale.

It is important to note that while the definition of the SCL basin as a collection of microstates is quite straightforward, the same is not true for the MSCL subspace. Metastability is the statistical property of the dynamic trajectories associated with the microstates. This problem can be tackled by noting that large metastable-phase solid clusters transform to equilibrium through activated nucleation processes in their interiors similar to the mechanism in the bulk. Hence, while the thermodynamic driving force as well as the number of nucleation sites for solid–solid transformation increases with the size of the growing clusters, the rate of nucleation of the equilibrium solid phase may in fact decrease due to rising activation barrier. The latter comes about because of increasing misfit strain energy of equilibrium-phase inclusions inside growing metastable-phase clusters. The existence and extent of the region of long-lived metastable-phase solid clusters in liquid that constitute the core of the MSCL subspace can be determined effectively through the closed ensemble technique mentioned above, by which critical nuclei of different sizes are stabilized.

With its core region identified, the boundary of an MSCL subspace can be delineated through direct canonical MD simulations of small solid–cluster seeds. This procedure relies on subdivision of each SCL basin into a contiguous MSCL domain and a transient region that connects it to other basins. Trajectories that are initiated by nucleation of critical solid clusters inside the MSCL subspace overwhelmingly grow to large sizes without structural transformation. Those initiated in the transient regions have a finite chance of crossing over into other SCL basins. This is analogous to transition path sampling, where trajectories initiated near the saddle points of the potential energy landscape are equally likely to decay into one or the other of the basins of attraction connected to it. We find that phase transformations of the critical nuclei initiated in the transient regions proceed through far from equilibrium processes involving cross-nucleation of the new phase at the crystal–liquid interfaces. It is important to note that the identification of the transient region boundaries does not rely upon CNT (or any of its assumptions therein) and thus,

provides a general procedure for the construction of kinetic phase maps.

As a consequence of the above topology of the phase space of the undercooled liquid, as well as the one to one correspondence between the sizes of the critical nuclei and undercooling temperature, we can construct solidification–kinetic phase maps of the principal solid phases that grow out of the melt under different temperature and pressure conditions. In what follows, we outline a practical framework based on a combination of nonequilibrium MD simulations (44), free energy integrations, and multiphase equilibrium simulations, through which thermodynamic as well as kinetic phase diagrams can be constructed. This methodology is applied to a model Cu system described by a short-range semiempirical interatomic potential (45). It exhibits a rather complex phase diagram, shown in Fig. 1, with several solid phases present along the melt line. In the following, we develop the methodology to construct the kinetic phase map shown in Fig. 5, where the conditions under which freezing is dominated by the metastable–bcc phase are delineated. It is quite noteworthy how large the region of metastable-phase growth can be. We conclude this paper with an in-depth study of hexagonal close-packed (hcp) clusters in coexistence with the melt, demonstrating their unusual interface structures and phase transformations accompanied by growth-mode transitions. On this basis, a mechanism for interface-driven metastable-phase growth is presented.

Thermodynamic Phase Diagram

Fig. 1 shows the temperature–pressure phase diagram of the embedded atom method (EAM) model–Cu system. The melt line $T_m(P)$ has been obtained from two-phase (solid–liquid) coexistence simulations in the isobaric–isoenthalpic (NPH) ensemble (46–49). Details are described in *SI Appendix*. It is found that the equilibrium solid phase at T_m is fcc for pressures $P < 71.6$ GPa, hcp in the interval $71.6 < P < 85$ GPa, and bcc for $P > 85$ GPa. The phase diagram contains two triple points: one at 71.6 GPa and 3,320 K, where fcc, hcp, and liquid coexist, and one at 85 GPa and 3,598 K, where hcp, bcc, and liquid coexist. A third three-phase coexistence point exists at 79.5 GPa and 3,478 K, but it does not appear in the phase diagram shown in Fig. 1 because it falls inside the stability range of the hcp phase. At this pressure, the hcp phase melts at the slightly higher temperature of 3,487 K.

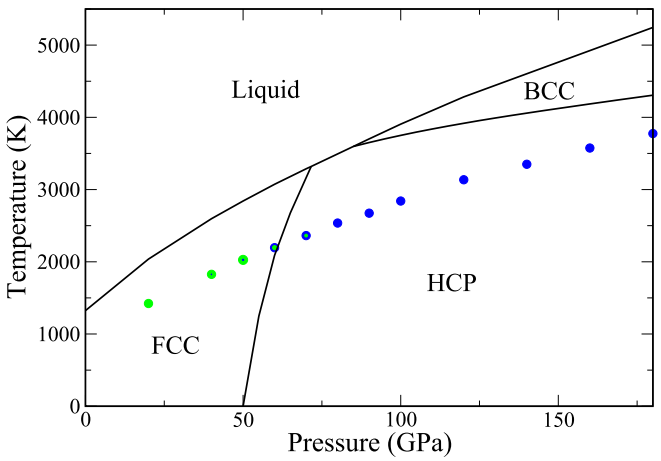

Fig. 1. Thermodynamic and ultrafast kinetic phase diagram. The black lines delineate the solid–liquid and solid–solid (bcc–hcp and fcc–hcp, respectively) coexistence curves. The colored filled circles show the temperature at which nucleation of solid from the melt was observed in direct MD simulations. The color indicates the dominant solid phase, with blue equal to bcc and green equal to close packed (fcc and/or hcp). In the pressure range 40 to 70 GPa, both phases are observed. The relative green to blue content of each symbol qualitatively depicts the prevalence of the bcc to the close-packed phases.

The solid–solid coexistence lines shown in Fig. 1 are drawn via integration of their slopes, given by the Clausius–Clapeyron relation, starting from the respective triple points. A detailed discussion of these calculations, as well as the latent heats and volumes of melting, is in *SI Appendix*.

Phase Map of Ultrarapid Solidification

In contrast to the thermodynamic melt line, which delineates the boundary between the liquid and solid phases in the limit of infinitely slow change of thermodynamic variables, we explore in this section the maximal effect of kinetics, by determining the start temperature T_{HS} for freezing with vanishing nucleation barrier. We have measured $T_{\mathrm{HS}}(P)$ through nonequilibrium molecular-dynamics (NEMD) simulations of ultrarapid cooling at a rate of 100 K/ns (Fig. 1). We have tracked the solid-phase evolution during these NEMD simulations using the adaptive cutoff common neighbor analysis (a-CNA) (50–52) method, which allows for identification of the hcp, as well as the fcc and the bcc phases. Fig. 1 depicts by color the solid phases observed at each pressure, with blue depicting the bcc phase and green depicting the close-packed fcc/hcp phases. At 80 GPa and above, pure bcc nucleation is observed, and the bcc nuclei grow and dominate the simulation box. Similarly, at pressures below 40 GPa, pure fcc nucleation is observed, and the close-packed nuclei grow and dominate the simulation box. In the pressure region between 40 and 70 GPa, polymorphic solidification takes place in the simulations. The difference in the observed polymorphic evolution kinetics as pressure is increased from 40 to 70 GPa is quite noteworthy. At 40 GPa, small bcc as well as close-packed (fcc/hcp) nuclei are formed, but the bcc nuclei quickly transform to close-packed phases and vanish. At 60 GPa, pure bcc nuclei do form and grow. However, transformation to close-packed phases during growth is also observed (Fig. 2). In this scenario, at first, small bcc nuclei form. During their growth stage, at or near the bcc solid–liquid interface, transformation to close-packed phases occurs, which starts competing with the original bcc phase as the nucleus grows.

It should be noted that T_{HS} at all pressures is clearly outside the region of thermodynamic stability of the bcc phase. Nevertheless, at pressures 80 GPa and above, not only nucleation occurs in the bcc phase, but the bcc nuclei grow to fill the simulation box. Hence, the solidification process kinetically stabilizes the metastable bcc phase. At pressures below 80 GPa, mixed close-packed and bcc nucleation as well as bcc to close-packed transformation of the growing nuclei can be observed. Hence, the NEMD simulations provide proof for polymorphic solidification kinetics near the triple point of the phase diagram. In the following, we analyze the physical origin of this phenomenon and discuss the conditions for growth of macroscopic-sized metastable bcc crystals, observable in laboratory experiments.

SCL Basins and Thermodynamics of Multiphase Metastable Equilibria

In this section, we discuss the prevalence of solid–liquid metastable equilibria. Multiphase simulations in the NPH ensemble constitute an effective tool for exploring the cores of the MSCL subspaces. Fig. 3 show examples of compact solid-phase nuclei that coexist with the liquid in the pressure range 20 to 100 GPa. They range from single-phase bcc, fcc, or hcp clusters to multiphase mixed fcc/hcp nuclei. These basins are distinct and weakly coupled to each other. It should be noted that the bulk bcc phase becomes thermodynamically stable above 85 GPa. Nevertheless, bcc clusters containing at least several thousand particles can be found stable in MD simulations with durations in the range of 5 to 10 ns, down to 20 GPa. This indicates that phase transformation of these clusters is clearly an activated

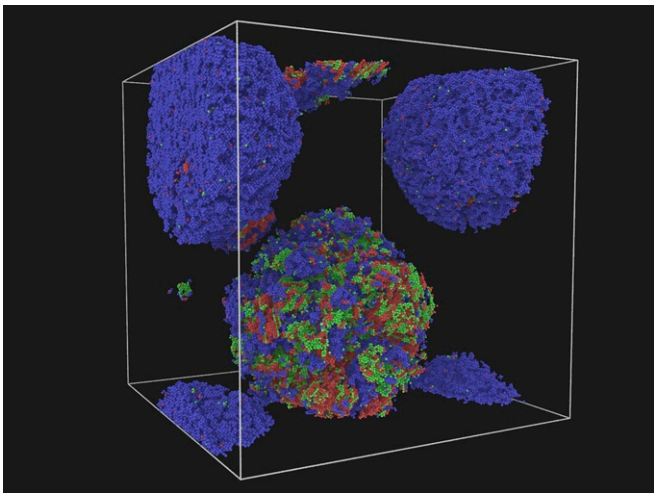

Fig. 2. A snapshot of an NEMD simulation during solidification at 60 GPa. Particles have been classified as belonging to different crystal phases via the a-CNA method (50–52): bcc (blue), fcc (green), and hcp (red). Particles identified as liquid have been removed.

process with a substantial barrier, which only increases with cluster size since nucleation of a new solid phase involves misfit strain that is easier to accommodate in smaller clusters interfacing the isotropic liquid. Hence, these solid–liquid equilibria constitute the core regions of their respective MSCL subspaces. It should however be noted that most shallow SCL basins may lack metastable subspaces. As is laid out in some detail in *SI Appendix*, we have not been able to stabilize mixed bcc/close-packed clusters in coexistence with the melt.

The study of metastable-phase cluster–liquid equilibria (Fig. 3) reveals many surprising structural features. For instance, in contrast to previous works in Lennard–Jones systems (29, 30, 36), where the fcc clusters were found to interface the liquid through a bcc shell, negligible structural heterogeneities are found at the solid–liquid interfaces for either fcc or bcc clusters in this study. However, when examining the hcp clusters (Fig. 3*C*), we find that the hcp-(0001) facets interface the liquid through a shell of fcc-(111) layers. This amounts to a shift in the stacking of the close-packed layers of hcp clusters, in favor of the fcc symmetry, in the vicinity of the melt. It is shown in *SI Appendix* that the energy cost associated with the change in stacking of the solid layers is an order of magnitude smaller than the fcc–liquid interfacial free energy. Later in this paper, we discuss a kinetic mechanism that drives the growth of metastable–fcc phase at (0001)-hcp–liquid interfaces at all temperatures below the fcc melting point. This behavior is quite at odds with the other hcp–liquid interface orientations. It lends credence to the unusual hcp–liquid interface structure, seen in Fig. 3*C*, as well as the existence of distinct MSCL basins of multiphase solid clusters composed of mixed fcc/hcp stackings (see Fig. 3*D*).

We conclude this section by pointing out that the existence of a multitude of MSCL basins demands that we quantify their relative thermodynamic stabilities or in other words, their phase space volumes. In the next section, we derive a rigorous and surprisingly general and convenient framework for extracting free energies of solid–liquid metastable equilibria from macroscopic observables extracted from equilibrium two-phase simulations, utilizing the one to one correspondence between the sizes and the coexistence temperatures of equilibrium solid clusters in

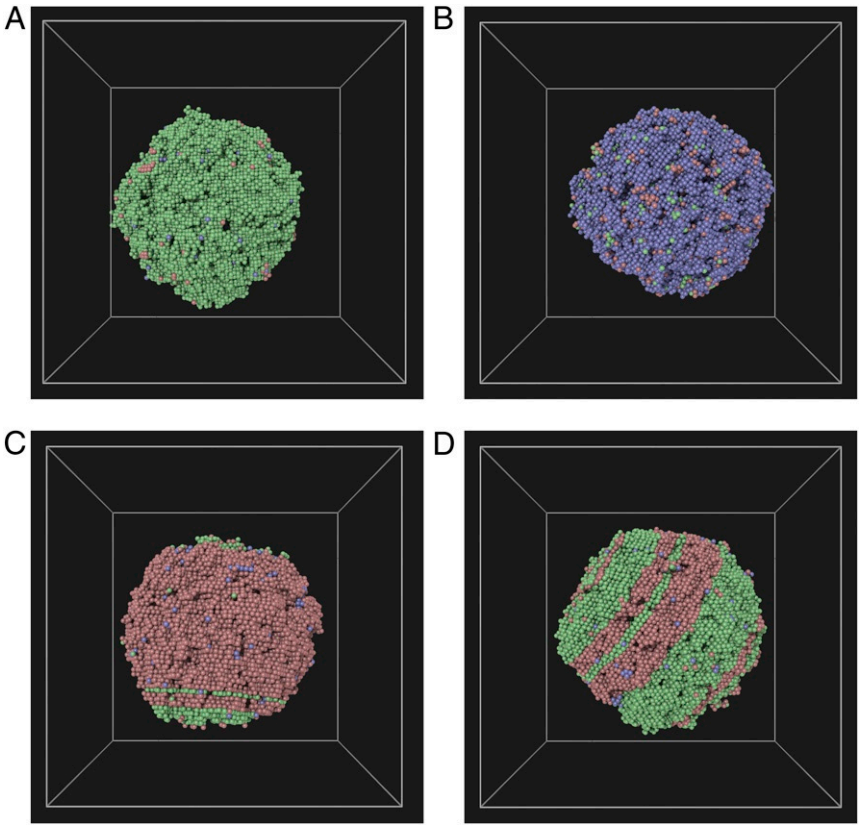

Fig. 3. *A–D* show four different crystal-phase clusters that can coexist in metastable equilibria with the liquid phase. Color coding is based on phase designation of each particle through the a-CNA method: fcc (green), bcc (blue), and hcp (red).

the melt. It makes no assumption regarding the equilibrium shapes of the crystalline nuclei or the complexity of their crystal structures. Later in this paper, the power of this methodology is demonstrated by applying it to computer simulations of the fcc and the bcc-phase MSCLs of the EAM–Cu model. Consequently, the relative prevalence of these phases during the different stages of the nucleation and the growth processes is quantified. Furthermore, the validity of several standard phenomenological rules that are commonly used to analyze kinetics of solidification in experiments is discussed.

Solid–Liquid Systems Thermodynamics. In the following, we describe a general and convenient methodology for directly extracting interfacial thermodynamic parameters from expectation values of macroscopic observables in computer or real-world experiments. We start by constructing the thermodynamic potential of a two-phase solid–liquid system at equilibrium in a closed ensemble (e.g., NPH) containing N_{sys} particles at overall pressure P and enthalpy $H_{\rm sys}$. We propose a subdivision of this system into a region of bulk solid surrounded by bulk liquid and separated by an interfacial region. This system is equilibrated at a uniform temperature T, which is controlled by the ensemble enthalpy $H_{\rm sys}$. The thermodynamic potential can thus be written as

$$G_{\rm SL}(T,P)=\min_{N_{\rm S}}\left[N_{\rm S}G^{\rm b}_{\rm S}(T,P)+N_{\rm L}G^{\rm b}_{\rm L}(T,P)+\gamma_I\left(N_{\rm S},T,P\right)\right], \quad [1]$$

where $N_{\rm S}$ and $N_{\rm L}$ are the numbers of the solid and the liquid particles, respectively; $G^{\rm b}_{\rm S}$ and $G^{\rm b}_{\rm L}$ are the bulk single-phase solid and liquid free energies, respectively; and γ_I is the interfacial free energy integrated over the interface area. While $G_{\rm SL}(T,P)$ is the property of a real physical system, its subdivision into parts is not unique. It is convenient to choose the interface to be an infinitely thin boundary with no associated volume and containing no particles. In this way, $N_{\rm S}$ and $N_{\rm L}$ can be determined from the conditions

$$N_{\rm S}+N_{\rm L}=N_{\rm sys}, \quad [2]$$

$$N_{\rm S}v_{\rm S}(T,P)+N_{\rm L}v_{\rm L}(T,P)=V_{\rm sys}, \quad [3]$$

where $v_{\rm S}$ and $v_{\rm L}$ are the bulk liquid- and solid-specific volumes, respectively, and $V_{\rm sys}$ is the system's volume. The above equations are particularly useful for extracting the average cluster size in MD simulations of solid–liquid equilibria, as will be described later in this paper.

It is profitable to express the interfacial free energy γ_I as

$$\gamma_I(N_{\rm S},P,T)=(N_{\rm S})^{\frac{2}{3}}\gamma_{\rm GT}(T,P)\kappa(N_{\rm S},T,P), \quad [4]$$

where $\gamma_{\rm GT}$ is the interfacial free energy of a fictitious unit cluster (i.e., one containing only one solid particle) in the so-called GT limit and $\kappa(N_{\rm S},T,P)$ is introduced to incorporate finite cluster-size curvature effects beyond the GT approximation. In this limit, the interfacial free energy integrated over the cluster surface area can be expressed in spherical coordinates as

$$\gamma_{\rm GT}(T,P)=\int\gamma_\infty\left(\hat{n}(\Omega);T,P\right)R^2(\Omega;T,P)\,d\Omega. \quad [5]$$

Above, $\hat{n}(\Omega)$ is the crystal surface normal of the interface element at Ω, and $\gamma_\infty(\hat{n};T,P)$ is its interfacial free energy density if it were extended in all directions. The equilibrium shape of this cluster $R_{\rm eq}(\Omega)$ is obtained by minimization of Eq. **5** with respect to $R(\Omega)$ under the constraint that the cluster volume is $v_{\rm S}$. This is an accurate physical description of large clusters. The equilibrium shape in the GT limit can be solved for analytically (53), with the Wulff construction as solution. For our purposes, the most important feature of Eq. **5** is that its equilibrium shape is independent of cluster size, and hence, γ_{GT} has the desirable property that it does not explicitly depend on $N_{\rm S}$. It is important to note that this does not require $R_{\rm eq}(\Omega)$ to be conserved when system is undercooled. The GT equilibrium shape can change when γ_∞ changes with temperature. Nevertheless, from variational point of view, γ_{GT} is only a function of temperature and pressure.

In contrast, for smaller clusters, the interfacial free energy density becomes a nonlocal functional of the crystal plane orientations $\hat{n}$ in the neighborhood of each surface element. In the simplest cases, there will be functional dependence on $\nabla\hat{n}$ to account for cluster surface curvature. This is the origin of the curvature coefficient κ, introduced in Eq. **4**, and its explicit dependence on cluster size $N_{\rm S}$. For large clusters, $\kappa(N_{\rm S}\to\infty,T,P)=1$.

The equilibrium/critical cluster size $N^c_{\rm S}$ can now be obtained by minimizing the thermodynamic potential G with respect to $N_{\rm S}$:

$$N^c_{\rm S}(T,P)=-\frac{2}{3}\frac{T_m}{\Delta H_m}\frac{\gamma_I}{\Delta T}\left(1+\frac{3}{2}N^c_{\rm S}\frac{\partial\log\kappa}{\partial N_{\rm S}}\right), \quad [6]$$

where ΔH_m is the latent heat and $\Delta T=T-T_m$ is the degree of undercooling from the melting temperature T_m, and we have used the relation

$$G^{\rm b}_{\rm S}(T,P)-G^{\rm b}_{\rm L}(T,P)=\frac{\Delta H_m}{T_m}\Delta T, \quad [7]$$

which is correct to first order in expansion about T_m. Note that Eq. **6** establishes a direct relationship between the observables $N_{\rm S}$ and ΔT through the total interfacial free energy γ_I and the curvature coefficient κ. The latter can be neglected for large clusters, as the following Taylor expansion can be made:

$$\kappa(N_{\rm S}\gg1)=1+\frac{\kappa^{(1)}}{(N_{\rm S})^{\frac{1}{3}}}+\ldots. \quad [8]$$

The above implies that $\frac{\partial\log\kappa}{\partial N_{\rm S}}$ in Eq. **6** can be neglected for large clusters. Furthermore, the combination of Eqs. **6** and **8** constitutes a rigorous formalism for determination of the interfacial free energy beyond the GT limit, incorporating the effect of temperature and pressure as well as finite cluster sizes.

In this section, we have thus devised a general framework for direct extraction of interfacial free energy per atom from experimental measurements of a system's volume, temperature, and pressure by using Eqs. **2**, **3**, and **6**. No severe assumptions or uncontrolled approximations are made, and the framework can be generalized to multicomponent as well as multiphase solid nuclei. Furthermore, finite-sized curvature effects beyond the GT limit can also be accounted for. Finally, it is worth noting that for systems where the specific volumes of solid and liquid phases are nearly indistinguishable, the condition of zero interface volume (Eq. **3**) can be replaced by a more appropriate order parameter, such as energy or bond-orientational order. Nonetheless, for most systems, the simplest order parameters for distinguishing the solid from the liquid phase will be adequate.

Phenomenological Models. When studying rapid solidification experiments for the purpose of identifying the conditions that lead to kinetics-driven phase selections, in contrast to predictions based on equilibrium thermodynamics, it is essential to have accurate models of multiphase thermodynamics. One of the most important developments in this regard is Turnbull's phenomenological rule (54) for solid–liquid interfacial free energies, which he showed to hold for a diverse collection of materials (mainly

metals). This rule can be generalized to an exact ansatz, at least in the GT limit, as follows:

$$\gamma_I = (\alpha_\epsilon - T\alpha_\sigma)\frac{\Delta H_m}{v_S^{2/3}} A_I^{\text{sphere}}. \quad [9]$$

Above, A_I^{sphere} denotes the interfacial area of an equisized spherical cluster, ΔH_m is the latent heat of solidification, v_S is the specific volume of the solid at temperature T, and α_ϵ and α_σ are dimensionless quantities that incorporate all temperature dependence as well as shape effects beyond that of a sphere. The conventional Turnbull coefficient is $\alpha(T_m) = \alpha_\epsilon - T_m\alpha_\sigma$.

Turnbull's remarkable rule conjectures that the solid–liquid interfacial tension scales as the difference in heat content of the solid and the liquid phases at the melting point. As a result, the dimensionless Turnbull coefficient $\alpha(T_m)$ is expected to be nearly independent of material chemistry. However, Turnbull found from experimentally inferred nucleation rates that for most metals, $\alpha(T_m) \approx 0.45$, while for nonmetals, $\alpha(T_m) \approx 0.32$ (54). Furthermore, variation of about 20% was predicted theoretically between the Turnbull coefficients of the fcc and the bcc crystal phases based on a polytetrahedral structural model of a liquid in contact with a rigid solid (55–57). It should be noted that extracting homogeneous nucleation rates from experiments is a daunting task, as solidification in most cases is driven by heterogeneous processes, and error bars are usually very large. It is thus desirable to use computer experiments to quantitatively study this conjecture.

The temperature dependence of the Turnbull coefficient, to first order in deviation from the melting point, is determined by the entropic contribution α_σ. Nelson and Spaepen (58) have argued that the origin of the solid–liquid interfacial tension is mainly entropic, whereupon they proposed the so-called negentropic model according to which the interfacial tension is all entropic (i.e., $\alpha_\epsilon = 0$). Since γ_I must necessarily be positive, this entails a negative interfacial entropy, thereof the name negentropic. The negentropic model in combination with Turnbull's rule has been widely used to analyze rapid solidification experiments (10).

Validation by Computer Experiments. We now show that while Turnbull coefficients $\alpha(T_m, P)$ have distinct values for different phases, such as bcc and fcc, they are nearly constant over a wide range of pressures in a typical metal. Furthermore, by explicit calculations of the interfacial energy α_ϵ, we calculate the entropic contribution to the interfacial free energy and demonstrate the accuracy of the negentropic model.

In order to calculate the Turnbull coefficients of the fcc and the bcc phases, we have conducted careful calculations of fcc–liquid and bcc–liquid equilibria in the pressure range from 60 to 100 GPa. For these studies, cubic simulation boxes, containing in excess of 13 million atoms, have been utilized. At each pressure, three two-phase systems at different H_{sys} are equilibrated for 8 ns each using NPH MD simulations with a time step of 2 fs, and the coexistence temperatures T_c and the systems' volumes V_{sys} are recorded. The coexistence temperatures T_c range from 30 to 60 K undercooling below T_m. The measured values of T_c and V_{sys} are inserted into Eqs. **2** and **3** to obtain N_S, which in turn, is used in Eq. **6** to obtain the interfacial free energy $\gamma_I(T_c, P)$. The latter is further used in Eq. **9** for evaluation of $\alpha(T_c, P)$, with $A_I^{\text{sphere}} = (36\pi)^{1/3}(N_S v_S)^{2/3}$. At each pressure, the calculated $\alpha(T_c, P)$ are fitted to a linear temperature dependence, which is used to estimate $\alpha(T_m, P)$.

Fig. 4*A* shows $\alpha(T_m)$ in the pressure range from 60 to 100 GPa for both the bcc and the fcc phases. To within the statistical accuracy of our calculations, $\alpha(T_m, P)$ for both phases can be considered nearly pressure independent, with $\alpha^{\text{fcc}}(T_m, P) \approx 0.54$ and $\alpha^{\text{fcc}}(T_m, P) \approx 0.465$. While this result confirms that the Turnbull coefficient of the fcc phase exceeds that of the bcc phase, their ratio of about 1.16 is significantly smaller than was found in ref. 59; Sun et al. (59) calculated the Turnbull coefficients of fcc and bcc iron using different empirical potential models and found α^{fcc} to be in the range from 0.5 to 0.55 in agreement with this work, but they found α^{bcc} to be in the range from 0.29 to 0.36, which is significantly smaller, leading to a ratio in excess of 1.5. Our result, however, is in closer agreement with the calculated relative Turnbull coefficients of the fcc and the bcc phases according to the polytetrahedral structural model of the liquid (55–57), as well as particle systems interacting via inverse power law potentials (60, 61). We thus conclude that the value of the Turnbull coefficient for a crystal phase can be quite sensitive to particle interactions. Nevertheless,

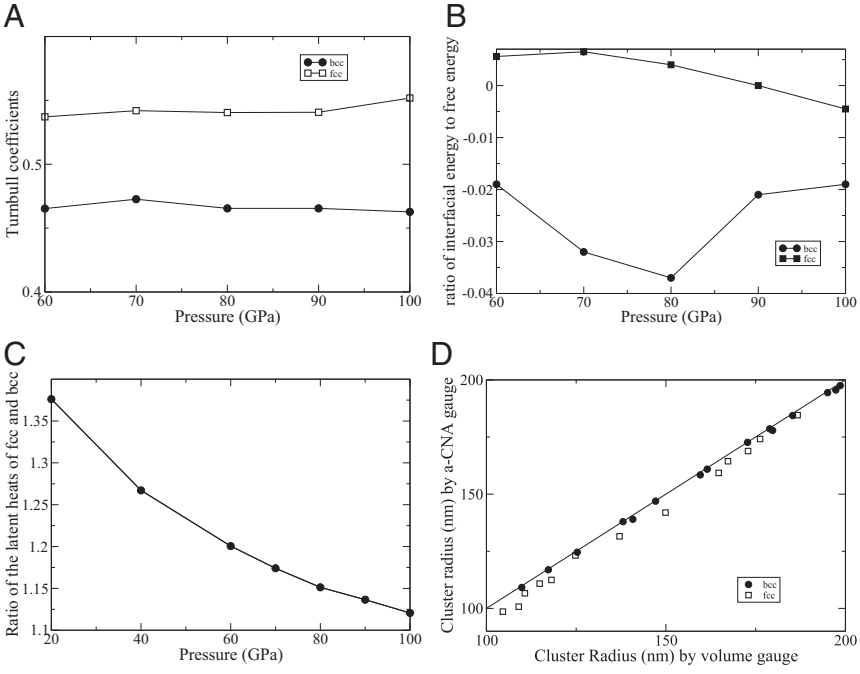

Fig. 4. (*A*) Calculated Turnbull coefficients for the fcc and the bcc phases as a function of pressure. (*B*) Ratio of the interfacial energy α_ϵ to the interfacial free energy $\alpha(T_m)$ of the fcc and the bcc phases as a function of pressure. (*C*) Ratio of the latent heats of the fcc and the bcc phases as a function of pressure. (*D*) Comparison of two different algorithms (gauges) for extracting cluster radii from MD simulations. The filled circles are bcc-cluster radii extracted from two-phase simulations at different temperatures and pressures ranging from 60 to 100 GPa. The open squares are fcc-cluster radii extracted from two-phase simulations at different temperatures and pressures ranging from 60 to 100 GPa.

we find the pressure dependence of the Turnbull coefficient to be weak, in agreement with a recent study of flat fcc–liquid interfaces (62).

It should be noted that the preferential nucleation of the bcc phase at large undercoolings is driven by the interfacial free energy, which depends both on the relative Turnbull coefficients as well as the relative latent heats of the bcc and the fcc phases. The latter are shown in Fig. 4*C*, where it is observed that $\Delta H_m^{fcc} > \Delta H_m^{bcc}$. Their ratio is, however, strongly pressure dependent. It is reduced from 1.37 at ambient pressure to 1.12 at 100 GPa. Nevertheless, at all pressures the larger latent heat and the larger Turnbull coefficient of the fcc phase contribute to $\gamma^{fcc} > \gamma^{bcc}$.

In order to discuss the temperature dependence of the Turnbull coefficient, we calculate the energetic contribution α_ϵ as follows:

$$\alpha_\epsilon \frac{\Delta H_m}{v_S^{2/3}} A_I^{\text{sphere}} = H_{\text{sys}} - N_S^c H_S^b - (N - N_S^c) H_L^b, \qquad [10]$$

where H_S^b and H_L^b are the bulk enthalpies of the solid and the liquid phases. Fig. 4*B* shows the ratio $\frac{\alpha_\epsilon}{\alpha(T_m)}$ for both the fcc and the bcc phases in the pressure range from 60 to 100 GPa. Clearly, the energetic part of α is very small, which validates the negentropic model for a typical metal. Also note that the bcc–liquid interfacial energy is negative and smaller than the fcc–liquid energy. The negative interfacial energy poses no conceptual problems, as it is much smaller in magnitude than the interfacial entropy. As a result, the interfacial free energy stays positive. It should further be noted that a prior study of flat solid–liquid interfaces of the Lennard–Jones system found that the entropic content of the interfacial free energy can vary significantly between interface orientations as well as densities (63). Hence, the validity of the negentropic model may be system dependent and hence, should be considered on a case by case basis.

We conclude this section by exploring different gauges for determining the cluster size N_S. We have until now only used the zero-volume gauge, which assumes the interface is infinitely thin. This gauge is convenient to use and applicable to any multiphase system with the coexisting phases having distinct specific volumes. In order to reduce the statistical error, elaborate order parameters have been devised in the literature that allow for accurate characterization the solid region within the liquid in two-phase systems. We have used one such method, described previously in ref. 41, as an alternative to the zero-volume gauge for determining N_S. In this method, the phase character of each particle is first determined by the a-CNA (50–52). Next, a coordination filter based on a radial distribution function is applied to remove atoms not belonging to the solid cluster. Finally, an effective radius for the cluster is determined by identifying its surface through Voronoi analysis. Fig. 4*D* shows the comparison between the radii R_S calculated in this way and those calculated using the zero-volume gauge and the relation $R_S = \left(\frac{3}{4\pi} N_S v_S\right)^{1/3}$. The figure shows effective cluster radii extracted from a number of two-phase simulations of bcc- and fcc-phase clusters coexisting with liquid at different pressures and temperatures. Overall agreement is quite impressive. It is, however, interesting to note that the agreement between the two methods for the bcc cluster radii is clearly better than for the fcc ones. Furthermore, the common neighbor analysis seems to slightly underestimate the effective radii of the fcc-phase clusters compared with the zero-volume gauge. It is important to reiterate that the absolute value of the interfacial free energy is subject to the chosen gauge. The only gauge-invariant physical observables are the total system's free energy, enthalpy, temperature, pressure, and volume. Therefore, it is important to use a consistent gauge when, for example, comparing the free energies of fcc- and bcc-phase nuclei coexisting with the liquid phase at a particular temperature and pressure.

Metastable–Solid Phase Diagrams

We are now ready to develop a general strategy for predicting kinetic stabilization of metastable crystal phases during solidification. For this purpose, we need to 1) quantify the relative phase stabilities of critical nuclei as a function of undercooling and 2) determine for each phase the extent of the MSCL basin or in other words, the range of solid-phase cluster sizes that can be considered metastable. In this way, we can predict the rate of transition from homogeneous undercooled liquid into any particular MSCL basin as a function of undercooling. As a result, we can identify the conditions that lead to metastable-phase growth by recognizing that whenever solidification occurs on a timescale shorter than the rate of transition out of an MSCL basin, the critical nuclei that belong to this basin are likely to grow to large sizes. To demonstrate the efficacy of this procedure, we apply it in the following two sections to the problem of metastable bcc-phase growth from the melt at pressures below 85 GPa, where one of the close-packed phases (fcc or hcp) is thermodynamically stable below the melting temperature (Fig. 1). It should be noted that in the vicinity of the hcp–fcc thermodynamic phase boundary (Fig. 1), stacking-fault free energies become so small that solidification into pure fcc or hcp phase becomes improbable. We conclude this paper with a discussion of intricacies arising from unusual structural features of hcp–liquid interfaces that promote mixed hcp/fcc-phase growth.

Solid–Nucleation-Phase Boundaries. In this section, we describe the procedure for determining the undercooling temperature $T^*(P)$, below which the nucleation rate of the metastable bcc phase exceeds those of the fcc and the hcp phases of EAM–Cu. Above this temperature, nucleation is dominated by the close-packed phases (fcc, hcp, or a combination thereof) and below it, by the bcc phase. Within the CNT, the rate of nucleation of critical solid clusters at temperature T_c is

$$J_S(T_c) = \sqrt{\frac{\Delta G_S''(T_c)}{2\pi k_B T_c}} \left(N_S^c(T_c)\right)^{2/3} \frac{\tau}{v_L} \exp\left(-\frac{\Delta G_S(T_c)}{k_B T_c}\right). \qquad [11]$$

Above, ΔG_S is the excess free energy of a critical solid nucleus coexisting with the melt at temperature T_c, and $\Delta G_S''$ is its curvature with respect to cluster size fluctuations. ΔG_S can be defined in terms of the quantities in Eq. **1**: $\Delta G_S = G_{SL} - N_{sys} G_L^b$, which were numerically determined in previous sections. τ denotes the rate of attachment from the liquid to a unit area of the solid cluster, and v_L is the specific volume of the liquid.

Eq. **11** allows the nucleation-phase boundary $T^*(P)$ to be determined by solving two equations: $J_S^{bcc}(T_{fcc}^*) = J_S^{fcc}(T_{fcc}^*)$ and $J_S^{bcc}(T_{hcp}^*) = J_S^{hcp}(T_{hcp}^*)$. Hence, the phase boundary $T^*(P)$ at any given pressure is the smaller of the two solutions T_{fcc}^* and T_{hcp}^* of the equations

$$G_{SL}^{cp}(T_{cp}^*) - G_{SL}^{bcc}(T_{cp}^*) = \frac{k_B T_{cp}^*}{2} \log\left[\frac{\Delta H_m^{cp} \alpha^{cp}}{\Delta H_m^{bcc} \alpha^{bcc}} \left(\frac{\tau^{cp}}{\tau^{bcc}}\right)^2\right], \qquad [12]$$

where T_{cp}^* represents either of the two temperatures T_{fcc}^* or T_{hcp}^*. We have solved the above equations by making two assumptions: 1) $\tau^{cp} \approx \tau^{bcc}$ and 2) $\alpha^{hcp} \approx \alpha^{fcc}$. These are both reasonable assumptions. Assumption 1 is good since the rate of attachment is mainly a property of the liquid. If desired, it can be calculated from size fluctuations of the critical clusters as described in refs. 64 and 65. We have found this unnecessary in the present

context because we have found that neglecting the right-hand side of Eq. **12** altogether only leads to a slight rise in $T^*(P)$. This increase is largest at low pressures. At 20 GPa, it amounts to 0.7 K, while at 40 GPa, it is reduced to only 0.25 K. Assumption 2 is reasonable due to the similarity of the two close-packed phases both structurally and energetically. In the pressure range of interest (around 70 GPa), we find that the latent heats of melting of the hcp and the fcc phases differ by only 2%, while that of the bcc phase is 20% smaller. Furthermore, their respective equilibrium shapes shown in Fig. 3 *A* and *C* suggest that $\alpha_{\mathrm{hcp}} > \alpha_{\mathrm{fcc}}$. This assertion is based on two observations: 1) the equilibrium shapes of fcc clusters in the melt are nearly spherical, from which it can be concluded that the fcc–liquid interfacial free energy only depends weakly on fcc crystal plane orientations, and 2) the equilibrium shapes of hcp clusters in the melt exhibit hcp-(0001) facets that interface the liquid through a shell of fcc-(111) layers. This implies that the liquid–fcc interfaces are favored relative to liquid–hcp ones and thus, have lower free energies.

Eq. **12** and its solutions are discussed in detail in *SI Appendix*. The resulting phase boundary $T^*(P)$, separating the temperature–pressure regions where bcc nucleation dominates $[T < T^*(P)]$ from those where fcc or hcp nucleation prevails $[T > T^*(P)]$, is shown in Fig. 5. At pressures $P < 71.9$ GPa, $T^*(P)$ (green line) is the nucleation phase boundary between the bcc and the fcc phases, and at $P > 71.9$ GPa (red line), it constitutes the boundary between the bcc- and the hcp-phase critical nuclei. Whenever a critical nucleus belongs to an MSCL basin, it is expected to be long lived. It can thus grow to large sizes and be observed during solidification and likely even after the phase transformation has completed. In the next section, we determine the extent of the bcc–MSCL basin upon very strong undercooling by studying the kinetic stability of postcritical bcc nuclei.

Before ending this section, we remark on the fcc–hcp–bcc critical nucleation triple point at $P = 71.9$ GPa and $T^* = 3{,}263$ K.

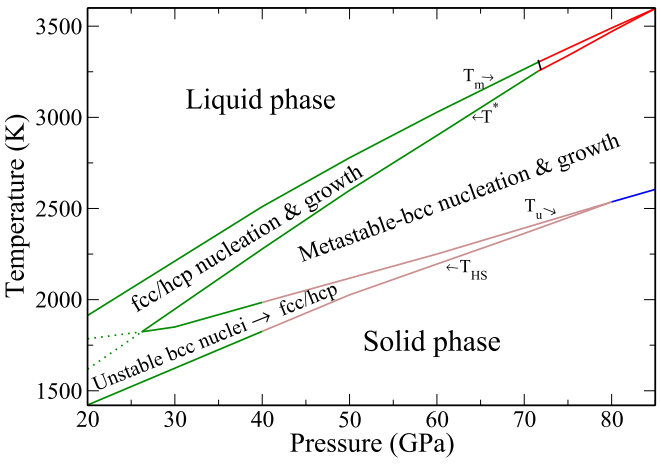

Fig. 5. A solidification–kinetic phase map. The top and bottom solid lines bound the region where solidification can take place. The four lines in order from top to bottom are 1) the thermodynamic melt line T_m, with the green part depicting liquid/fcc-phase boundary and the red part depicting liquid/hcp; 2) the boundary T^*, where the CNT rate of bcc nucleation equals the fcc rate (green part) or the hcp rate (red part) with a critical nucleation bcc–hcp–fcc triple point at $P = 71.9$ GPa and $T = 3{,}263$ K; 3) the boundary T_u, below which the postcritical bcc nuclei become unstable and transform to fcc (green part) and mixed fcc/hcp (brown part); and 4) the boundary T_{HS}, below which the liquid phase becomes unstable and crystallization occurs with vanishing nucleation barrier and thus, can be observed in MD simulations. The colors depict the observed crystal phase in the simulations: fcc: green; mixed fcc/hcp: brown; and bcc: blue. The solid parts of the T^* and T_u lines bound the region, where the bcc phase is nucleated inside the bcc–MSCL subspace.

The line connecting this point in Fig. 5 to the bulk thermodynamic fcc–hcp–liquid triple point at $P = 71.6$ GPa and $T_m = 3{,}320$ K is the boundary that separates the temperature–pressure regions where nucleation (according to the CNT) is dominated by the fcc phase from those where the hcp phase is most favored. However, we expect kinetic factors beyond those considered in this section to promote mixed fcc/hcp solidification at $T > T^*(P)$ within at least a 10-GPa-wide pressure window about the thermodynamic triple point at $P = 71.6$ GPa, due to diminishing energy cost of stacking faults. At first sight, this may seem only marginally relevant to solidification kinetics and have little effect on the liquid–solid interfacial kinetics. However, we will show in a later section that in regions where the CNT predicts hcp-dominated nucleation and growth, the liquid interface with special hcp plane orientations can in fact promote fcc-phase growth by a kinetic mechanism.

Kinetic Phase Stabilities of Postcritical Nuclei. In the previous section, we computed the phase line $T^*(P)$, below which critical nucleation is dominated by the bcc phase. In this section, we determine the conditions for the bcc postcritical nuclei to grow to large sizes without transforming to other solid phases. Hence, we quantify the temperature–pressure region within which critical nucleation occurs inside the bcc–MSCL subspace. The weak coupling of the MSCL subspace to other basins guarantees growth of postcritical nuclei without solid–solid transformation. In contrast, the transient regions of the SCL basins contain postcritical clusters that may undergo structural instabilities. The extent of the transient subspace can be studied straightforwardly via NEMD simulations in the isobaric–isothermal (NPT) ensemble by 1) preparing atomistic configurations of critical solid-phase clusters embedded in the melt at different undercooling temperatures, 2) initiating dynamic trajectories from these configurations, and 3) characterizing the evolution of their solid-phase content as the solid clusters grow. The approach we have chosen to pursue for accomplishing the above tasks is detailed in *SI Appendix*. We have carefully applied this procedure to examining the kinetic stability of postcritical bcc nuclei at pressures 20, 30, 40, and 60 GPa. Our aim has been to identify the undercooling temperatures $T_u(P)$, below which the growing bcc nuclei transform to fcc/hcp phases. In other words, the critical nuclei smaller than N_u do not belong to the bcc–MSCL basin, as they readily transform to fcc/hcp when growing. The result is shown in Fig. 5, where the $T_u(P)$ line is green below 40 GPa and brown below 80 GPa. This coloring is intended to convey the fact that at temperatures below T_u, in the green pressure region the unstable bcc nuclei are observed to transform to close-packed structures dominated by the fcc phase (*SI Appendix*, Fig. S9), while in the brown region, multiphase fcc/hcp clusters are observed (*SI Appendix*, Fig. S7). Of course, there is no sharp boundary between the two regions, and the hcp content of the multiphase region rises with increasing pressure. At 80 GPa, T_u and T_{HS} coincide, and solidification at all undercoolings is found to be dominated by the bcc phase. This has been proven by direct NEMD simulations, which consistently show bcc nucleation and stable growth at $P \geq 80$ GPa under ultrarapid cooling conditions.

It is beneficial here to discuss in some detail the physical meaning of the temperatures $T_u(P)$. They designate the lowest undercooling at which all of the computationally prepared bcc nuclei that could grow under this condition grow without transforming to other solid phases. This does not exclude that at lower temperatures, there may exist bcc clusters that can grow without transformation to close-packed phases. This rather conservative measure of metastability is justified if we seek to predict the conditions for experimental observations of macroscopic-sized solid phases. For this purpose, it should be recognized that our computer experiments are quite limited in their representation of the perturbations that can occur in realistic

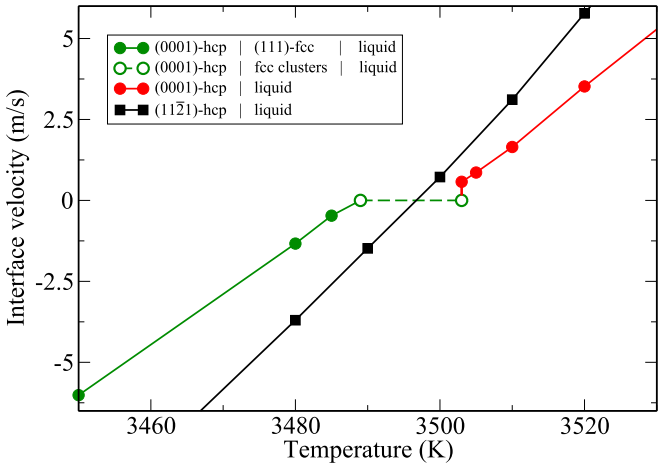

Fig. 6. Temperature dependence of the mobility of two different hcp–liquid planar interfaces with orientations (0001) and (11$\bar{2}$0) at pressure $P = 80$ GPa and $T_m = 3{,}497$ K. The calculations are performed in periodic slab geometries, with dimensions specified in *SI Appendix*. The (0001) interface kinetics is partitioned into three temperature regimes. 1) $T < 3{,}489$ K (green solid line with filled circles): The liquid phase transforms to the fcc phase, which grows on the hcp substrate. 2) $3{,}489 \leq T \leq 3{,}503$ K (green dashed line with open circles): No steady-state interface motion is observed. The hcp substrate interfaces the liquid through a film of fluctuating fcc clusters. 3) $T \geq 3{,}503$ K (red solid line with filled circles): The hcp slab melts at steady rate.

experiments. Nevertheless, examination of the ultrarapid solidification snapshot at 60 GPa, shown in Fig. 2, confirms the formation of bcc nuclei at the start of solidification, some of which transform to close-packed phases during early growth, with the close-packed content increasing with time.

It is instructive to briefly discuss the states at the boundary between the bcc–MSCL domain and the transient region. *SI Appendix*, Fig. S9 shows an example of a solid critical cluster at 30 GPa on the verge of dynamic stability. It contains about $N_u \approx 200$ particles identified by a-CNA to mainly have bcc symmetry. This cluster was obtained by slowly shrinking a metastable bcc cluster in the NPH ensemble. When growing this cluster at 1,860 K in the NPT ensemble, it transitions to the fcc phase, while at 1,863 K, it grows to large sizes as bcc. This result is reproducible from different initial configurations, demonstrating the boundary of the bcc–MSCL subspace. It should be noted that the critical clusters at large undercoolings are far from compact and spherical, and their kinetics cannot be described within the CNT framework, which is better suited for the slower kinetics at small undercoolings.

We conclude this section by pointing out that here we have only scratched the surface of a vast phenomenology pertaining to kinetic stability of solid clusters growing within undercooled liquids. We have touched upon the growing bcc clusters in EAM–Cu, which transform to fcc at large undercoolings. This instability is conventionally expected to be due to the vibrational instability of the bulk bcc phase under these conditions. However, we show in *SI Appendix* that far from equilibrium conditions caused by fast interface kinetics can drive solid–solid phase transformations in growing clusters with stable bulk phonons. This mechanism is explicitly nonequilibrium and interface driven, and it cannot be explained by the dynamical structural properties of the bulk crystal phase alone.

Extraneous-Phase Interface Layers: Interfacial Phase Transformations Coupled to Growth-Mode Transitions

Hitherto in this paper, we have discussed kinetic stabilization of metastable single-phase bcc solid at significant undercooling. This is the expected regime based on Ostwald's step rule, which suggests that small solid clusters in liquid can prefer phases other than the bulk equilibrium phase, due to their interfaces with the melt contributing substantially to their stability. As an example, the line representing $T^*(P)$ in Fig. 5 depicts the minimal undercooling required for nucleation of metastable–bcc phase from the melt for the model Cu system of this study. In this analysis, the interface assumes a passive role. As described earlier in this paper, it suffices to consider the interface as a dividing surface occupying no space and containing no particles, only contributing to the overall free energy of solid nuclei immersed in the melt. This is reasonable as long as the internal structure of the solid–liquid interface can be neglected.

However, the observation of hcp nuclei with heterogeneous interface structures (Fig. 3*C*) is suggestive of the existence of such phenomenology that cannot be explained via the above approach. In particular, Fig. 3*C* shows that the (0001)-hcp planes interface the liquid via an fcc shell. This can be rationalized by the observation that the stacking fault free energy is an order of magnitude smaller than the solid–liquid interfacial free energy (*SI Appendix*).

The observation of a shell structure is not new. In fact, in the earliest computational studies (29) of the Lennard–Jones system, the fcc nuclei were found to be coated by bcc layers at their interfaces with the melt. To our knowledge, the ramifications of this unusual interfacial structure for the kinetics of solidification have not been explored in the literature. As mentioned earlier, we have not been able to observe such bcc shell structures in any of our systems, which suggests that the energy cost of fcc–bcc interfaces must be relatively high in our systems. However, the fcc shell structure at the interface of hcp-(0,001) planes with the melt offers an opportunity to study its unusual features.

Unusual internal structures of solid–liquid interfaces in finite-sized nuclei (e.g., Fig. 3*C*) inevitably bring forth the question of whether such atomic arrangements are dependent on the interfacial curvature. If so, structural transformations are to be expected at the interfaces of the growing solid nuclei. This is undoubtably a noteworthy phenomenon with possible deep ramifications for crystal growth kinetics. If not the case, the shell structure should appear even in the flat interface limit. In the following, we present an in-depth study of this limit by two-phase simulations of periodic slab geometries for two interface orientations, hcp-(0,001) and hcp-(1,1$\bar{2}$0), in the neighborhood of the melting point $T_m = 3{,}497$ K at 80 GPa, where hcp is the bulk equilibrium phase (Fig. 1). Based on our previous discussions of Fig. 3*C*, the hcp-(0001) interface with the liquid should be in the fcc phase, contrary to the hcp-(11$\bar{2}$0) interface that stays isostructural with the bulk phase (*SI Appendix*, Fig. S11). A systematic study of the dynamic properties of these solid–liquid configurations at small undercooling and superheating reveals the remarkable result shown in Fig. 6. It depicts the velocity of each interface as a function of temperature in the vicinity of T_m; positive sign of the velocity indicates growing liquid phase, and negative sign implies solid-phase growth. In the narrow range of temperatures studied in Fig. 6, about 1% deviation from T_m, linear response is expected. This is clearly observed for the hcp-(11$\bar{2}$0) interface mobility in Fig. 6. Note that due to the relatively small latent heat of the EAM–Cu system (i.e., $\Delta H/k_B T_m \approx 1$), which is typical of simple metals, the interface is atomically rough, and crystal growth is dominated by rates of attachment and detachment of atoms to the crystal surfaces that are controlled by liquid diffusivity, often only thermal velocity, and the latent heat (66). The available sites for attachment on the rough interfaces are large, commonly assumed to be about 1/4 of all of the sites, so-called repeatable step sites (67).

In contrast, the (0001) interface velocity has strongly nonlinear temperature dependence. In particular, in the interval $\Delta_a = (3{,}489, 3{,}503)$ K, interface mobility vanishes on the

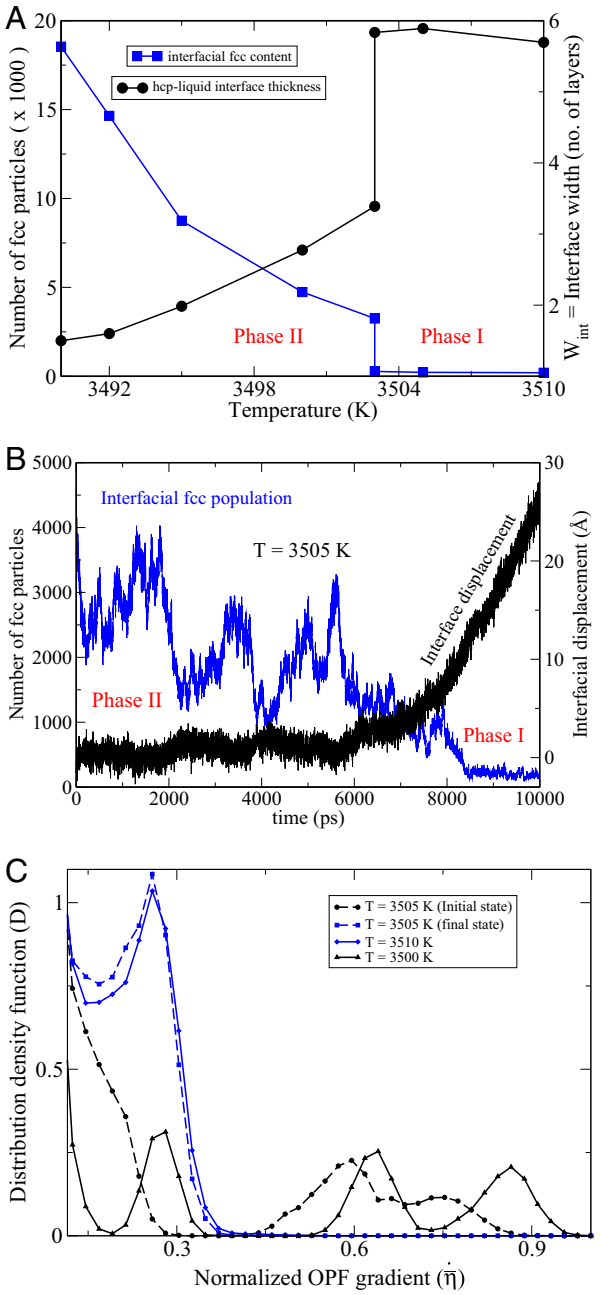

Fig. 7. (*A*) The blue curve depicts the number of fcc particles in the system that mainly reside near the (0001)-hcp–liquid interfaces, and the black curve shows the interface widths W_{int} as a function of temperature. (*B*) Time evolution of an NPT MD simulation at $T = 3{,}505$ K, initiated from an (0001)-hcp–liquid equilibrium slab configuration at $T = 3{,}500$ K. The blue line shows the evolution of the number of fcc particles, while the black line represents for the same simulation the displacements of the (0001)-hcp–liquid interfaces as a function of time, derived from the size fluctuations of the simulation box. The symmetry character of the particles have been identified via the common-neighbor analysis using a cut-off radius of 2.875 Å. (*C*) The distribution density function $D(\bar{\eta})$. The blue curves depict the distribution functions of the phase I atomically rough interfaces with relatively small OPF gradients, and the black curves show the sharp phase II interfaces with much higher OPF gradients. The dashed lines have been obtained by averaging over the first and the last 2,000 time steps of the simulation shown in *B*.

simulation timescale exceeding 10 ns (dashed green line in Fig. 6). Outside of this interval, interface motion is observed to be normal, diffusive, and linearly changing with temperature variations. Above 3,503 K, the hcp phase shrinks smoothly at a speed proportional to the superheating, as shown in Fig. 6 as well as in *SI Appendix*, Fig. S13. Below 3,489 K, the interface region is solid fcc and grows steadily at a speed proportional to the undercooling from the fcc melting point at 3,489 K (Fig. 6 and *SI Appendix*, Fig. S14).

Fig. 7*A* explains the sudden dynamical arrest of the (0001) interface, observed at 3,503 K in Fig. 6, by invoking a first-order structural-phase transformation at the interface. The order parameter for this transformation is the fcc content of the interface. Above 3,503 K, the concentration of the fcc particles at the interface is dilute, which we designate as phase I. It undergoes a discontinuous jump at 3,503 K, transitioning to phase II, in which larger fcc clusters form and dissolve (*SI Appendix*, Fig. S12). While the rate of attachment to the fcc sites on the underlying hcp substrate is high, the clusters cannot become critical as long as the temperature is above the fcc melting point of 3,489 K. Further cooling toward the latter temperature causes the fcc content at the interface to steadily rise. As shown in *SI Appendix*, Fig. S11, the thicknesses of fcc-containing films at the interface are smallest near the transition temperature ($\approx$ 3,503 K) and increase upon cooling. Below 3,489 K, metastable fcc phase grows on the (0001) interface.

An important feature of first-order phase transformations is the presence of hysteresis, which implies that metastable phases exist in the vicinity of the transformation temperature. This is confirmed by NPT MD simulations at $T = 3{,}503$ K, which can equilibrate in either phase I or II depending on initiation. In contrast, Fig. 7*B* clearly demonstrates that phase II is unstable at 3,505 K. It shows the time evolution of the fcc population at the interface in an NPT MD simulation starting from a configuration in phase II (large fcc content) generated at 3,500 K. During the course of the simulation, the fcc clusters dissolve, and the interfacial structure transforms to phase I (*SI Appendix*, Fig. S15). Similarly, we find that phase I is unstable at 3,501.5 K. Hence, the hysteresis window is at most 2 GPa.

Fig. 7*B* also records the motion of the interface with time. The intimate coupling of the interfacial structure to its dynamics is clearly evidenced in this figure. The fcc shell at the interface seems to constitute a protective shield for the hcp substrate, which starts dissolving at around 7,000 ps, when the fcc population has dwindled.

In order to explain the coupling mechanism between interfacial structure and its dynamics, we study the atomic roughness of the hcp–liquid interfaces at different temperatures. It correlates strongly with the width of an interface, which in turn, can be quantified by the extent of the region, where an order parameter field (OPF) exhibits large gradients. In the following, we outline a rigorous method for measuring interfacial thickness from atomistic simulations. As a result, we prove that hcp–liquid interfaces undergo an atomically diffuse to sharp transition concurrent with the structural transformation from phase I to phase II. Consequently, the growth mode changes abruptly from continuous (fast) to layer by layer with high nucleation barrier.

We choose as the order parameter the fraction of the particles in a volume element that are designated via the common-neighbor analysis as hcp. Let $\eta(z)$ be the OPF along the hcp-(0001) plane normal, and define the OPF gradient $\dot{\eta}(z)$ as the derivative of this function. It is now straightforward to define and calculate the distribution of OPF gradients from the simulations. For this purpose, it is convenient to work with normalized OPF gradients: $\bar{\dot{\eta}}(z) = \dot{\eta}(z)/\dot{\eta}_{\max}$, where $\dot{\eta}_{\max} = \eta_{\text{hcp}}/\Delta z_{\text{hcp}}$, with η_{hcp} being the value of the order parameter in bulk hcp solid and Δz_{hcp} being the interlayer spacing of the hcp-(0001) planes. The physical representation of $\dot{\eta}_{\max}$ is a maximally sharp interface, with a bulk solid layer next to a liquid layer with negligible order. We can now define the distribution density function $D(\bar{\dot{\eta}})$ in the interval $0 < \bar{\dot{\eta}} < 1$, normalized by the relation

$$\int_0^1 D(\dot{\bar{\eta}})\ d\dot{\bar{\eta}} = \frac{L_{\text{slab}}}{\Delta z_{\text{hcp}}}, \qquad [13]$$

where L_{slab} is the length of the simulation box along the (0001) plane normal. $D(\dot{\bar{\eta}})\ d\dot{\bar{\eta}}$ is the number of layers with OPF gradients in a $d\dot{\bar{\eta}}$ window around $\dot{\bar{\eta}}$. The hcp–liquid interface layer thickness can now be calculated as

$$W_{\text{int}} = \frac{1}{2}\int_{\dot{\bar{\eta}}_{\text{min}}}^1 D(\dot{\bar{\eta}})\ d\dot{\bar{\eta}}. \qquad [14]$$

The factor $1/2$ above stems from the necessary presence of two interfaces in any periodic supercell, and $\dot{\bar{\eta}}_{\text{min}}$ is obtained from the equation

$$\frac{1}{2}\int_{\dot{\bar{\eta}}_{\text{min}}}^1 D(\dot{\bar{\eta}})\ \dot{\bar{\eta}}\ d\dot{\bar{\eta}} = 1 - \frac{\eta_{\text{liq}}}{\eta_{\text{hcp}}}. \qquad [15]$$

The left-hand side of the above equation integrates over all of the intermediate layers (i.e., interfacial region) that are required to transition from the highest order parameter value η_{hcp} in the bulk solid to the lowest one in the liquid. It derives from two considerations: 1) the interfacial region is confined to the spectral domain with the highest OPF gradients, and 2) the interface is sandwiched between the solid region with the order parameter η_{hcp} and the liquid region with the order parameter η_{liq}. In our systems, $\eta_{\text{liq}}/\eta_{\text{hcp}} \approx 0.0004$ and thus, is negligible.

The result of the above analysis is shown in Fig. 7*A*, where a discontinuous drop in hcp–liquid interface thickness W_{int} is observed upon phase transformation. Fig. 7*C* shows the density functions $D(\dot{\bar{\eta}})$ for a few interfaces belonging to the two different phases. It is clear that upon transformation from phase I to phase II, the interface becomes smooth and planar and grows layer by layer through two-dimensional nucleation with large activation barrier so that the interfacial motion halts within the computational time scale of this study.

We conclude this section by noting that the structural anisotropy of the hcp phase gives rise to heterogenous growth patterns. In particular, in the system studied here, a growing hcp cluster always contains smooth (0001) facets, on which only metastable fcc phase can grow (Fig. 3*C*). At the same time, other hcp–liquid interface orientations behave normally and promote the growth of the hcp phase. Hence, interfacial kinetics can drive the growth of multiphase nuclei. This explains the prevalence of mixed fcc–hcp clusters in the pressure range from 60 to 80 GPa (Fig. 3*D*).

Discussion

In this paper, we have conducted an in-depth study of the kinetic processes during solidification that stabilize crystal phases that are not thermodynamically stable in the bulk. At the nucleation stage, these phases are stabilized by their relatively low interfacial free energies. Additionally, at the growth stage, the kinetic barrier to structural transformation is high and therefore, makes any transition to the thermodynamic ground state improbable. This happens most prominently near the triple points of the phase diagram. By constructing a polymorphic nucleation theory from atomistic first principles and by conducting a rigorous study of the kinetic stability of postcritical nuclei during their growth stage, we have successfully managed to devise a rational framework for characterizing and quantifying the conditions for nucleation and growth of metastable crystal phases during solidification. As a result, in addition to the regular thermodynamic phase diagram, we also construct a kinetic phase diagram that delineates the temperature–pressure regions where metastable phases are favored to grow from the melt.

As a proof of concept, we have applied the above methodology to an atomistic system described by a model EAM–Cu interatomic potential. We thus construct a metastable phase map complementing the thermodynamic phase diagram of this system (Fig. 5). It is quite sobering to observe the significant extent of the metastable region. It is bounded from above by the solid-nucleation phase boundary $T^*(P)$ and from below by $T_u(P)$, under which the growing bcc nuclei become kinetically unstable. The procedure adopted in this paper assumes near-equilibrium critical nuclei, whose thermodynamic as well as kinetic stabilities are investigated. However, no simplifying assumptions regarding their shapes or structures are made. No doubt, more sophisticated studies of the nonequilibrium kinetics during nucleation are necessary to determine the domain of validity of the assumption of near-equilibrium nuclei (68).

It should be noted that kinetic phase maps are not universal. They depend on the kinetic mechanism that is being considered. Conventionally, kinetic stabilization of metastable phases has been discussed as a result of phase selection during the nucleation stage described within the CNT. In this picture, thermodynamic driving forces govern the phase of a critical nucleus, which according to the CNT, grows to large sizes no fail. In this way, kinetic phase diagrams can be drawn and be interpreted just like thermodynamic phase diagrams. In this paper, we have generalized this idea by including kinetics in a restrictive way as to preserve the notion of a phase diagram. For this purpose, we have introduced the concept of SCL basins and their MSCL subspaces, defined as subdomains of the former that are weakly connected to other SCL basins. Hence, nucleation from the undercooled liquid into a particular MSCL subspace with near certainty is guaranteed to evolve without further phase transformations. The real power of this idea lies in the realization that MSCL subspaces contain all of the large clusters since the barrier to nucleation of solid–solid transformations only increases with cluster size. Hence, if critical nucleation occurs in the transient region of the SCL basin, unless kinetic instabilities occur within a short time after, the nucleus inevitably grows large enough to transition to the MSCL subspace. Hence, thermodynamic conditions that lead to nucleation into the MSCL subspace can be easily identified by exclusion of all those that lead to a finite number of clusters undergoing kinetic instabilities amid their early growths.

While the above is quite a reasonable guiding principle for construction of solidification–kinetic phase diagrams, it is too restrictive and sweeps all real complexities aside by excluding them from the MSCL subspaces. This shortcoming becomes apparent after the growth of metastable fcc in competition with an anisotropic crystal phase such as hcp is considered. In this case, the solid–liquid interface cannot be treated as uniform. Rather, there are special interfaces, whose behaviors are radically different from others. These interfaces can have complex structures distinct from the bulk of the solid clusters and can undergo phase transformations, which in turn, induce sharp transitions in the growth kinetics of competing crystal phases in their neighborhoods. Due to this explicit role of interfacial structure and dynamics, different crystal orientations may promote growth of disparate crystal phases. As a result, the fundamental notion of the kinetic phase boundary as an infinitely thin dividing surface in analogy with the thermodynamic phase boundary must be abandoned and generalized.

Materials and Methods

In this paper, we have presented results of a series of large-scale MD simulations using the LAMMPS code (44) and the EAM interatomic potential for Cu metal, as constructed by Mishin et al. (45). This model represents the bulk physical properties of Cu quite well at ambient condition. While it is not fitted to high-pressure ab initio data, it constitutes a reasonable model for atomic interactions in a generic close-packed metal under pressure. When not otherwise specified, simulations were performed with a 1-fs time step. Visualization and analysis of simulation snapshots were carried out using the OVITO

program package (69). Solid-phase designation of each particle has been done via a-CNA (50–52). Particles are colored according to their phase designation: fcc phase (green), bcc phase (blue), and the hcp phase (red).

Data Availability. All study data are included in the article and/or *SI Appendix*.

ACKNOWLEDGMENTS. B.S. and J.L.B. are grateful for the guidance, insights, and support from Prof. Russell Hemley. We acknowledge Alex Chernov, Lorin Benedict, Sebastien Hamel, and Amit Samanta for helpful discussions. We also thank A. Arsenlis, D. P. McNabb, B. K. Wallin, and R. S. Maxwell for project support. This work was performed under the auspices of the US Department of Energy by Lawrence Livermore National Laboratory Contract DE-AC52-07NA27344.

1. W. Ostwald, Studien Über die Bildung und Umwandlung Fester Körper. *Z. Phys. Chem.* **22**, 289–330 (1897).
2. I. N. Stranski, D. Totomanow, Keimbildungsgeschwindigkeit und Ostwaldsche Stufenregel. *Z. Phys. Chem.* **163**, 399–408 (1933).
3. C. Guo, J. Wang, J. Li, Z. Wang, S. Tang, Kinetic pathways and mechanisms of two-step nucleation in crystallization. *J. Phys. Chem. Lett.* **7**, 5008–5014 (2016).
4. G. I. Toth, J. R. Morris, L. Granasy, Ginzburg-Landau-type multiphase field model for competing fcc and bcc nucleation. *Phys. Rev. Lett.* **106**, 045701 (2011).
5. R. E. Cech, Undercooling of Fe-Ni droplets. *Trans. AIME* **206**, 585–589 (1956).
6. Y. Liu, H. Nie, R. Bansil, M. Steinhart, J. Bang, T. P. Lodge, Kinetics of disorder-to-fcc phase transition via an intermediate bcc state. *Phys. Rev. E* **73**, 061803 (2006).
7. J. Bang, T. P. Lodge, Long-lived metastable bcc phase during ordering of micelles. *Phys. Rev. Lett.* **93**, 245701 (2004).
8. S. Xu, H. Zhou, Z. Sun, J. Xie, Formation of an fcc phase through a bcc metastable state in crystallization of charged colloidal particles. *Phys. Rev. E* **82**, 010401(R) (2010).
9. P. Tan, N. Xu, L. Xu, Visualizing kinetic pathways of homogeneous nucleation in colloidal crystallization. *Nat. Phys.* **10**, 73–79 (2014).
10. D. M. Herlach, Non-equilibrium solidification of undercooled metallic melts. *Metals* **4**, 196–24 (2014).
11. D. M. Herlach, Containerless undercooling and solidification of pure metals. *Annu. Rev. Mater. Sci.* **21**, 23–44 (1991).
12. C. Notthoff, B. Feuerbacher, H. Frans, D. M. Herlach, D. Holland-Moritz, Direct determination of metastable phase diagram by synchrotron radiation experiments on undercooled metallic melts. *Phys. Rev. Lett.* **86**, 1038–1041 (2001).
13. O. Shuleshova, W. Löser, D. Holland-Moritz, D. M. Herlach, J. Eckert, Solidification and melting of high-temperature materials: In situ observations by synchrotron radiation. *J. Mater. Sci.* **47**, 4497–4513 (2012).
14. S. Klein, D. Holland-Moritz, D. M. Herlach, Crystal nucleation in undercooled liquid zirconium. *Phys. Rev. B* **80**, 212202 (2009).
15. P. C. Myint, J. Belof, Rapid freezing of water under dynamic compression. *J. Phys. Condens. Matter* **30**, 233002 (2018).
16. D. Charbonneau *et al.*, A super-earth transiting a nearby low-mass star. *Nature* **462**, 891–894 (2009).
17. D. H. Dolan, Y. M. Gupta, Time-dependent freezing of water under dynamic compression. *Chem. Phys. Lett.* **374**, 608–612 (2003).
18. D. H. Dolan, Y. M. Gupta, Nanosecond freezing of water under multiple shock wave compression: Optical transmission and imaging measurements. *J. Chem. Phys.* **121**, 9050–9057 (2004).
19. D. H. Dolan, M. D. Knudson, C. A. Hall, C. Deeney, A metastable limit for compressed liquid water. *Nat. Phys.* **3**, 339–342 (2007).
20. M. Bastea, S. Bastea, J. E. Reaugh, D. B. Reisman, Freezing kinetics in overcompressed water. *Phys. Rev. B* **75**, 172104 (2007).
21. S. J. P. Stafford, D. J. Chapman, S. N. Bland, D. E. Eakins, Observations on the nucleation of ice VII in compressed water. *AIP Conf. Proc.* **1793**, 13005 (2017).
22. A. E. Gleason *et al.*, Compression freezing kinetics of water to ice VII. *Phys. Rev. Lett.* **119**, 025701 (2017).
23. P. C. Myint *et al.*, Nanosecond freezing of water at high pressures: Nucleation and growth near the metastability limit. *Phys. Rev. Lett.* **121**, 155701 (2018).
24. S. Alexander, J. P. McTague, Should all crystals Be bcc? Landau theory of solidification and crystal nucleation. *Phys. Rev. Lett.* **41**, 702 (1978).
25. M. J. Mandell, J. P. McTague, A. Rahman, Crystal nucleation in a three-dimensional Lennard-Jones system. II. Nucleation kinetics for 256 and 500 particles. *J. Chem. Phys.* **66**, 3070–3075 (1977).
26. S. Nose, F. Yonezawa, Isothermal-isobaric computer simulations of melting and crystallization of a Lennard-Jones system. *J. Chem. Phys.* **84**, 1803–1814 (1986).
27. J. Yang, H. Gould, W. Klein, Molecular-dynamics investigation of deeply quenched liquids. *Phys. Rev. Lett.* **60**, 2665 (1988).
28. W. C. Swope, H. C. Andersen, 10^6-Particle molecular-dynamics study of homogeneous nucleation of crystals in a supercooled atomic liquid. *Phys. Rev. B* **41**, 7042–7054 (1990).
29. P. R. ten Wolde, M. J. Ruiz-Montero, D. Frenkel, Numerical evidence for bcc ordering at the surface of a critical fcc nucleus. *Phys. Rev. Lett.* **75**, 2714–2717 (1995).
30. P. R. ten Wolde, M. J. Ruiz-Montero, D. Frenkel, Numerical calculation of the rate of crystal nucleation in a Lennard-Jones system at moderate undercooling. *J. Chem. Phys.* **104**, 9932–9947 (1996).
31. G. M. Torrie, J. P. Valleau, Monte Carlo free energy estimates using non-Boltzmann sampling: Application to the sub-critical Lennard-Jones fluid. *Chem. Phys. Lett.* **28**, 578–581 (1974).
32. P. J. Steinhardt, D. R. Nelson, M. Ronchetti, Bond-orientational order in liquids and glasses. *Phys. Rev. B* **28**, 784–805 (1983).
33. J. S. van Duijneveldt, D. Frenkel, Computer simulation study of free energy barriers in crystal nucleation. *J. Chem. Phys.* **96**, 4655–4688 (1992).
34. Y. C. Shen, D. W. Oxtoby, Bcc symmetry in the crystal-melt interface of Lennard-Jones fluids examined through density functional theory. *Phys. Rev. Lett.* **77**, 3585–3588 (1996).
35. D. Moroni, P. R. ten Wolde, P. G. Bolhuis, Interplay between structure and size in a critical crystal nucleus. *Phys. Rev. Lett.* **94**, 235703 (2005).
36. C. Desgranges, J. Delhommelle, Controlling polymorphism during the crystallization of an atomic fluid. *Phys. Rev. Lett.* **98**, 235502 (2007).
37. Y. Huang, J. Wang, Z. Wang, J. Li, C. Guo, Y. Guo, Y. Yang, Existence and forming mechanism of metastable phase in crystallization. *Comput. Mater. Sci.* **122**, 167–176 (2016).
38. B. Groh, B. Mulder, Why all crystals need not be bcc: Symmetry breaking at the liquid-solid transition revisited. *Phys. Rev. E* **59**, 5613–5620 (1999).
39. S. Pan, S. Feng, J. Qiao, W. Wang, J. Qin, Crystallization pathways of liquid-bcc transition for a model iron by fast quenching. *Sci. Rep.* **5**, 16956 (2015).
40. M. Santra, R. S. Singh, B. Bagchi, Nucleation of a stable solid from melt in the presence of multiple metastable intermediate phases: Wetting, Ostwald's step rule, and vanishing polymorphs. *J. Phys. Chem. B* **117**, 13154–13163 (2013).
41. L. A. Zepeda-Ruiz, B. Sadigh, A. A. Chernov, T. Haxhimali, A. Samanta, T. Oppelstrup, S. Hamel, L. X. Benedict, J. L. Belof, Extraction of effective solid-liquid interfacial free energies for full 3D solid crystallites from equilibrium MD simulations. *J. Chem. Phys.* **147**, 194704 (2017).
42. X.-M. Bai, M. Li, Calculation of solid-liquid interfacial free energy: A classical nucleation theory based approach. *J. Chem. Phys.* **124**, 124707 (2006).
43. J. R. Espinosa, C. Vega, C. Valeriani, E. Sanz, Seeding approach to crystal nucleation. *J. Chem. Phys.* **144**, 034501 (2016).
44. S. Plimpton, Fast parallel algorithms for short-range molecular dynamics. *J. Comput. Phys.* **117**, 1–19 (1995).
45. Y. Mishin, M. J. Mehl, D. A. Papaconstantapoulos, A. F. Voter, J. Kress, Structural stability and lattice defects in copper: Ab initio, tight-binding, and embedded-atom calculations. *Phys. Rev. B* **63**, 224106 (2001).
46. G. J. Martyna, D. J. Tobias, M. L. Klein, Constant pressure molecular dynamics algorithms. *J. Chem. Phys.* **101**, 4177–4189 (1994).
47. M. Parrinello, A. Rahman, Polymorphic transitions in single crystals: A new molecular dynamics method. *J. Appl. Phys.* **52**, 7182–7190 (1981).
48. M. E. Tuckerman, J. Alejandre, R. Lopez-Rendon, A. L. Jochim, G. J. Martyna, A Liouville-operator derived measure-preserving integrator for molecular dynamics simulations in the isothermal-isobaric ensemble. *J. Phys. Math. Gen.* **39**, 5629–5651 (2006).
49. W. Shinoda, M. Shiga, M. Mikami, Rapid estimation of elastic constants by molecular dynamics simulation under constant stress. *Phys. Rev. B* **69**, 134103 (2004).
50. D. Faken, H. Jonsson, Systematic analysis of local atomic structure combined with 3D computer graphics. *Comput. Mater. Sci.* **2**, 279–286 (1994).
51. J. D. Honeycutt, H. C. Andersen, Molecular dynamics study of melting and freezing of small Lennard-Jones clusters. *J. Phys. Chem.* **91**, 4950–4963 (1987).
52. A. Stukowski, Visualization and analysis of atomistic simulation data with OVITO-the open visualization tool. *Model. Simulat. Mater. Sci. Eng.* **18**, 015012 (2010).
53. L. D. Landau, E. M. Lifshitz, *Statistical Physics* (Butterworth-Heinemann, ed. 3, 1980), vol. 5.
54. D. Turnbull, Formation of crystal nuclei in liquid metals. *J. Appl. Phys.* **21**, 1022–1028 (1950).
55. F. Spaepen, A structural model for the solid-liquid interface in monatomic systems. *Acta Metall.* **23**, 729 (1975).
56. F. Spaepen, R. B. Meyer, The surface tension in a structural model for the solid-liquid interface *scripta*. *Met. Mater.* **10**, 257–263 (1976).
57. C. V. Thompson, "Crystal formation in easy glass-forming metallic alloys," PhD thesis, Harvard University, Cambridge, MA (1979).
58. D. R. Nelson, F. Spaepen, "Polytetrahedral order in condensed matter" in *Solid State Physics*, H. Ehrenreich, D. Turnbull, Eds. (Academic Press, New York, NY, 1989), vol. 42, 1–90.
59. D. Y. Sun, M. Asta, J. J. Hoyt, M. I. Mendelev, D. J. Srolovitz, Crystal-melt interfacial free energies in metals: Fcc versus bcc. *Phys. Rev. B* **69**, 020102(R) (2004).
60. B. Laird, R. L. Davidchack, Direct calculation of the crystal-melt interfacial free energy via molecular dynamics computer simulation. *J. Phys. Chem. B* **109**, 17802–17812 (2005).
61. R. L. Davidchack, B. B. Laird, Crystal structure and interaction dependence of the crystal-melt interfacial free energy. *Phys. Rev. Lett.* **94**, 086102 (2005).
62. A. Samanta, J. Belof, The thermodynamics of a liquid-solid interface at extreme conditions: A model close-packed system up to 100 GPa. *J. Chem. Phys.* **149**, 124703 (2018).
63. B. Laird, R. L. Davidchack, Y. Yang, M. Asta, Determination of the solid-liquid interfacial free energy along a coexistence line by Gibbs-Cahn integration. *J. Chem. Phys.* **131**, 114110 (2009).
64. S. Auer, D. Frenkel, Numerical prediction of absolute crystallization rates in hard-sphere colloids. *J. Chem. Phys.* **120**, 3015–3029 (2001).
65. E. Sanz *et al.*, Homogeneous ice nucleation at moderate supercooling from molecular simulation. *J. Am. Chem. Soc.* **135**, 15008–15017 (2013).
66. K. A. Jackson, Current concepts in crystal growth from the melt. *Prog. Solid State Chem.* **4**, 53–80 (1967).
67. K. A. Jackson, The interface kinetics of crystal growth processes. *Interface Sci.* **10**, 159–169 (2002).
68. T. Kawasaki, H. Tanaka, Formation of a crystal nucleus from liquid. *Proc. Natl. Acad. Sci. U.S.A.* **107**, 14036–14041 (2010).
69. A. Stukowski, Structure identification methods for atomistic simulations of crystalline materials. *Model. Simulat. Mater. Sci. Eng.* **20**, 045021 (2012).

PNAS
www.pnas.org

Supplementary Information for

Metastable-solid phase diagrams derived from polymorphic solidification kinetics

Babak Sadigh, Luis Zepeda-Ruiz, Jonathan L. Belof

To whom correspondence should be addressed: Babak Sadigh, Jonathan L. Belof.
E-mail: sadigh1@llnl.gov, belof1@llnl.gov

This PDF file includes:

Supplementary text
Figs. S1 to S15
References for SI reference citations

Supporting Information Text

Thermodynamic phase diagram

The temperature-pressure phase diagram of the EAM model system has been directly calculated from two-phase (solid-liquid) coexistence simulations. For this purpose, we have performed simulations in an isobaric-isoenthalpic (NPH) ensemble (1–4). This can be considered a closed ensemble, as there is no energy exchange with an external bath, since the total system's enthalpy is kept fix. At the bulk melting point T_m, the free energies of the liquid and the solid phases are equal. However, the enthalpy of the solid H_S^m is lower than that of the liquid H_L^m. This discrepancy is observed in real-world experiments as latent heat $\Delta H_m = H_L^m - H_S^m$, released during the crystallization process. If the total enthalpy of the simulation cell H_{sys} is chosen in the range $H_S^m < H_{sys} < H_L^m$, the system will necessarily equilibrate into a solid-liquid coexistence. For an S-L coexistence with flat boundaries, it can readily be shown that the system temperature equilibrates at T_m (5). Such an S-L equilibrium can be established by designing an elongated computational cell, with H_{sys} chosen in the neighborhood of $1/2\,(H_S^m + H_L^m)$.

For the calculation of the fcc-liquid coexistence line, we have chosen computational cells containing 160,000 atoms, composed of $20 \times 20 \times 100$ primitive fcc unit cells with 4 atoms in each cell, which are arranged through stacking of fcc (001) layers. For the bcc-liquid line, computational cells containing 216,000 atoms have been used that are composed of $30 \times 30 \times 120$ primitive bcc unit cells with 2 atoms per cell, arranged through stacking of bcc (001) layers. The hcp-liquid coexistence line has been obtained via computational cells containing 83200 atoms, composed of $26 \times 50 \times 16$ hcp orthorhombic unit cells with 4 atoms per cell that are arranged by stacking hcp-$(11\bar{2}0)$ layers. The orthorhombic hcp unit cell has the lattice vectors: $\mathbf{a_1} = (0, 0, c/a)$, $\mathbf{a_2} = (1, 0, 0)$, $\mathbf{a_3} = (0, \sqrt{3}, 0)$. In the ideal hcp crystal $c/a = \sqrt{8/3}$.

Recall now that the free energies of non-pathological single-phase systems decrease monotonically with temperature, and the liquid free energy due to its larger entropy slopes down steeper than the free energy of any solid phase. Hence the free energy curves of the liquid and every solid phase ϕ cross at one and only one point T_m^ϕ. Consequently, the thermodynamic melting point T_m coincides with the highest T_m^ϕ.

It is thus found that the phase with the highest T_m is the fcc phase at $P < 71.6$ GPa, the hcp phase in the interval $71.6 < P < 85$ GPa, and the bcc at $P > 85$ GPa. Figure S1 shows the melt lines of the three phases bcc, fcc and hcp in the pressure range 40-100 GPa. We observe three triple points, one at 71.6 GPa and 3320 K, where liquid-hcp-fcc coexist, and one at 85 GPa and 3598 K, where liquid-hcp-bcc are at three-phase equilibrium. There also exists an fcc-bcc-liquid triple point at 79.5 GPa and 3478 K. It is slightly lower than the hcp melting point of 3487 K at this pressure, and therefore does not appear in the thermodynamic phase diagram, see Fig. 1 in the main text. Of course, these numbers are so close to each other that in practice, all four phases in the vicinity of 80 GPa can be considered thermodynamically stable.

A consequence of locating a triple point along the melt line is that it can be used as the starting point for integration of the phase boundary $T_{\rm cx}(P)$ of the two coexisting crystal phases P_1 and P_1, using the Clausius-Clapeyron relation, according to which, the slope of the phase boundary is related to the ratio of the latent volume to the latent heat of the transition between the two phase:

$$\frac{dT_{\rm cx}}{dP} = T_{\rm cx}\,\frac{\omega_{P_1} - \omega_{P_2}}{H_{P_1} - H_{P_2}}\bigg|_{T_{\rm cx},P} \qquad [1]$$

Above, ω_{P_1} and H_{P_1} denote the volume and the enthalpy per atom at pressure P and the coexistence temperature $T_{\rm cx}(P)$ for phase P_1.

We have calculated the hcp-bcc and the fcc-bcc phase boundaries by integration of Eq. 1 with 5 GPa and 10 GPa pressure increments respectively, Each equilibrium volume/enthalpy calculation involved averaging over a 1 ns MD-NPT simulation for the hcp-bcc and 2 ns for the fcc-bcc boundary, corresponding to 1000000 and 2000000 time steps respectively. The simulation supercells consisted of $20 \times 20 \times 20$ bcc unit cells (16000 atoms), $20 \times 20 \times 20$ fcc unit cells (32000 atoms), and $22 \times 13 \times 14$ orthorhombinc hcp unit cells (16016 atoms). Each integration started from the triple point of that boundary. They are shown in Fig. S1, as well as in Fig. 1 of the main text. The coexistence lines have substantial curvatures. The hcp-bcc line starting at 85 GPa, has a slope of nearly 11 K/GPa, which shrinks monotonically to about 6 K/GPa at 170 GPa. The fcc-bcc line has a smaller slope of 5.3 K/GPa at 80 GPa, which further decreases to 0.9 K/GPa at 120 GPa, and then rises again and exceeds 3 K/GPa at 160 GPa. The hardest phase boundary to calculate accurately is the fcc-hcp line, which is nearly vertical, due to the similarity of the two phases, and its calculation requires small preessure increments. Figure S2 shows the fcc-hcp energy differences per atom at 0 K, which exhibits a transition pressure of 50 GPa. In the same pressure range at 0 K, the bcc phase is much higher in energy: 0.0455 eV/atom above fcc at 0 GPa. This energy difference decreases only slightly with pressure. At 100 GPa, it becomes 0.0395 eV/atom.

Let us digress briefly here to discuss in some detail the algorithm we devised for efficient computation of the hcp-fcc coexistence line. As mentioned earlier, the two-phase simulations revealed an fcc-hcp-liquid triple point at 71.6 GPa and 3320 K. Performing equilibrium solid-phase simulations using the same fcc and hcp simulation cells as described above at this condition with simulation times of 2 ns, and using Eq. 1, we calculate the pressure-derivative of the hcp-fcc coexistence-line at the triple point $\dot{T}_{\rm cx}(71.6) = 101.36$ K/GPa. Combining this with the fcc-hcp energy difference at 0 K, which becomes zero at 50 GPa, see Fig. S2, we can make a first ansatz for the shape of the line:

$$T_{\rm cx}^{(0)}(P) = 3320 + 101.36\ (P - 71.6) - 2.42332\ (P - 71.6)^2. \qquad [2]$$

Next we improve the fidelity of this approximation by choosing an intermediate pressure, e.g. 60 GPa, where we calculate at several temperatures, e.g. 1876 K, 1990 K, 2036 K, 2448, the equilibrium volumes and enthalpies of the two phases and

plug into Eq. 1 to obtain four candidate phase-coexistence slopes at $P = 60$ GPa, which we denote in the following by $\dot{T}_{60}(T)$. Through a line fit to this data, we obtain the following equation for the dependence of the slope of the coexistence line at 60 GPa on the coexistence temperature

$$\dot{T}_{60}(T) = -64.6834 + 0.0969619T. \quad [3]$$

Note that $T_{\rm cx}^{(0)}(60) \approx 1818$. We now make an improved ansatz

$$T_{\rm cx}^{(1)}(P) = 3320 + 101.36\ (P - 71.6) + C\ (P - 71.6)^2 + D\ (P - 71.6)^3. \quad [4]$$

The two unknown coefficients C and D can now be determined by the two known relations: Eq. 3 and $T_{\rm cx}(50) = 0$. The result is $C = 1.9338$ and $D = 0.2017$. Consequently, $T^{(1)}(60) = 2090$. We chose to stop at this level. But this procedure can be continued for systematic improvement of the phase line.

We have also independently verified the fcc-bcc phase boundary calculated above at three pressures, 80, 120, and 180 GPa with thermodynamic integration from bcc to fcc along the Bain path. Good agreement between the two methods has been found.

For a more in-depth view of the multiphase thermodynamics of the EAM model-Cu system, we redraw its thermodynamic phase diagram in the temperature-density plane, see Fig. S3. Furthermore, the pressure dependences of the latent volumes and latent heats of melting are shown in Figs. S4 and S5. Note the discontinuous jumps at the triple points. In particular, the specific volume of the hcp phase is smaller than the fcc phase by about 0.14% at their triple point. At 0 K this discrepancy increases to nearly 0.3% at 70 GPa.

SCL basins and thermodynamics of multiphase metastable equilibria

It is interesting to note that pure bcc and fcc metastable clusters embedded in liquid are homogeneous single-phase solids both in their cores and at their interfaces with the melt. This is in contrast to previous studies of solidification in the Lennard-Jones system (6–8), where critical nucleation on the order of thousand atoms was induced by order-parameter-based (Q_6) umbrella sampling, and it was found that the fcc critical nuclei interface the liquid through a bcc shell. We have studied fcc and bcc nuclei coexisting with liquid at pressures ranging from 0 (20 for bcc) to 100 GPa, and sizes ranging from a few thousand to nearly a million. They are all nearly spherical in shape and exhibit negligible structural heterogeneity at the liquid-solid interfaces. However, when examining the hcp clusters, see Fig. 3(c) in the main text, we find that the hcp-(0001) facets interface the liquid by transforming to fcc-(111). The appearance of an fcc shell structure at the hcp/liquid interface for only certain orientations is a clear manifestation of strong hcp/liquid interfacial anisotropy.

In order to rationalize the fcc shell structure on the hcp-(0001) facets, we have calculated the stacking fault energies in the hcp phase at 0 K as shown in Fig. S6. It displays the energetics of an intrinsic and an extrinsic stacking fault in the hcp crystal. In order to understand the atomic arrangements in these structure, one needs to know that there is degeneracy in optimal stacking of close-packed planes of hard spheres. The hcp phase corresponds to the periodic AB stacking, and the fcc phase to the periodic ABC stacking. An intrinsic stacking fault in the hcp phase can be formed by the non-periodic ..ABABCBCB.. stacking of the (0001) planes, while an extrinsic stacking fault corresponds to inserting a C plane into the structure to obtain ..ABABCABAB.. The stacking fault energies shown in Fig. S6 are an order of magnitude smaller than the fcc-liquid interfacial free energies, which range from 382 ergs/cm^2 at 40 GPa to 525 ergs/cm^2 at 80 GPa, using the Turnbull coefficient of 0.54 as calculated in the main text. As was noted in the previous section, the volume mismatch between the hcp and the fcc stacking only descreases with temperature, and there is no reason to believe temperature will markedly incease the stacking fault free energies. We have nevertheless studied the stability of a periodic 7-layer extrinsic stacking fault approximant ABABCAB, at 80 GPa by calculating its melting point via two-phase simulations and comparing it with those of the hcp and the fcc phases. The periodic slab supercells used for these simulations contained 91000 atoms with similarly elongated shapes as previously described for hcp-liquid two-phase simulations. The calculated melting point for this structure was 3487 K, to be compared with the fcc melting point of 3489 K and the hcp melting point of 3497 K. This implies that the free energy cost of growing fcc shells in the interface region between an hcp substrate and the liquid is quite small. As a result, it is reasonable to expect that there exist MSCL basins that contain clusters composed of mixed fcc/hcp stackings in equilibrium with the liquid. An example of such a cluster is shown in Fig. 3(d) in the main text. It is important to note that these basins are distinct and weakly coupled to each other and to the single-phase MSCLs illustrated in Figs. 4(a)-(c) in the main text.

The main question that now arises is whether there are mixed bcc/closed-packed MSCL basins. While it is quite easy to imagine mixed bcc/close-packed configurations, such as shown in Fig. S7, we have not been able to find a solid-liquid metastable (long-lived) equilibrium with the solid phase comprised of close-packed and bcc regions in coexistence. The configuration shown in Fig. S7 was generated in a simulation box containing 314928 particles at 60 GPa that initially contained a pure bcc cluster at equilibrium with liquid in the NPH ensemble. The cluster was slowly shrunk by reducing the total enthalpy of the NPH ensemble until no discernible solid cluster was left in the simulation box. Then the ensemble was switched to NPT, and the temperature was dropped down to 2200 K, corresponding to the homogeneous nucleation start temperature T_{HS} at 60 GPa. Subsequently, nucleation and growth of a mixed bcc/fcc cluster occurred, which is shown in Fig. S7. Once the cluster size exceeded 30000 particles, the ensemble was switched back to NPH and the multiphase system was equilibrated for over 1 ns at 60 and 80 GPa. At 60 GPa, the bcc fraction of the cluster gradually vanished during relaxation. In contrast, equilibration of the mixed bcc/fcc/hcp cluster at 80 GPa, lead to gradual disappearance of the fcc and hcp parts, and eventually a pure bcc-liquid two-phase equilibrium was obtained. We thus conclude that while the mixed-phase bcc/close-packed clusters can be

generated by kinetic processes for short times, they are not metastable, and rather belong to the transient region between two MSCL basins.

Solid-nucleation phase boundaries

In order to better understand the structure of the solutions of Eq. 12 of the main text, we elaborate below on explicit expressions for its left-hand side. The right-hand side (RHS) is small and can be treated as a perturbation. We start by expressing the excess free energy $\Delta G_{\rm S}(N_{\rm S})$ of a solid-liquid equilibrium composed of a solid nucleus of size $N_{\rm S}$ embedded in the melt, by a first-order expansion in deviation of the undercooling temperature T from the melting point T_m (see Eq. 7 in the main text), and using the Turnbull ansatz for the interfacial free energy Eq. 9 of the main text:

$$\Delta G_{\rm S}(T) = N_{\rm S}\frac{\Delta H_m}{T_m}(T-T_m) + \left(36\pi N_{\rm S}^2\right)^{2/3}\frac{\Delta H_m}{{v_{\rm S}}^{2/3}}\alpha. \quad [5]$$

By combining the generalized Gibbs-Thomson relation Eq. 6 of the main text, with the Turnbull ansatz Eq. 9 of the main text, we obtain

$$N_{\rm S}(T) = \frac{32\pi}{3}\left(\frac{T_m\ \alpha}{T_m - T}\right)^3. \quad [6]$$

Inserting the above into Eq. 5, we find the following zeroth-order solution $T_{\rm cp}^{*(0)}$ of Eq. 12 in the main text, i.e. when its RHS is set to zero

$$\frac{T_{\rm cp}^{*(0)} - T_m^{cp}}{T_{\rm cp}^{*(0)} - T_m^{\rm bcc}} = \frac{T_m^{cp}}{T_m^{\rm bcc}}\sqrt{\left(\frac{\alpha_{cp}}{\alpha_{\rm bcc}}\right)^3\frac{\Delta H_m^{cp}}{\Delta H_m^{\rm bcc}}}. \quad [7]$$

The above represents the equation of the thermodynamic solid-solid (cp-bcc) phase-lines of the critical nuclei, with cp representing either of the closed-packed phases fcc or hcp. It requires the knowledge of the Turnbull coefficients, latent heats and melting temperatures of all phases of interest, in our case bcc, fcc, and hcp. All these quantities have been explicitly determined previously in this paper except $\alpha_{\rm hcp}$. It is expected to be very similar to $\alpha_{\rm fcc}$ but larger. We have solved Eq. 12 assuming $\alpha_{\rm hcp} = \alpha_{\rm hcp} = 0.54$, and the resulting $T_{\rm fcc}^*$ and $T_{\rm hcp}^*$ are shown as solid lines in Fig. S8. The nucleation phase line $T^*(P)$ is the minimum of $T_{\rm fcc}^*$ and $T_{\rm hcp}^*$ at every pressure, and is shown in Fig. 5 of the main text. The triple point pressure where $T_{\rm fcc}^* = T_{\rm hcp}^*$ is at 71.9 GPa, where $T^* = 3263$. Fig. S8 also shows how $T_{\rm hcp}^*$ change if $\alpha_{\rm hcp}$ is significantly increased to 0.56. This is shown by the dashed line in Fig. S8, where the triple point has now moved up to nearly 74 GPa. This constitutes a 2 GPa uncertainty in the location of the fcc-bcc-hcp coexistence point of the critical solid nuclei embedded in the melt.

Kinetic stability of postcritical clusters

We intend to study below the kinetic stabilities of postcritical nuclei by simulating their growth via MD simulations within the NPT ensemble. As described in the main text, this study involves three steps: (i) preparing atomistic configurations of critical solid-phase clusters embedded in the melt at different undercooling temperatures, (ii) initiating dynamic trajectories from these configurations, and (iii) characterizing the evolution of their solid-phase content as the solid clusters grow. The most difficult task is the preparation of critical clusters at large undercoolings. The method implemented here, which is described below, is only one of many approaches. Certainly bias-potential methods using bond-orientational order parameters as employed in the past in e.g. (6) and (9) can be quite effective in this regard.

For the present study we have followed the following protocol:

1. Start with a metastable bcc-liquid equilibrium in the core of the MSCL domain, obtained through the closed-ensemble (NPH) technique.

2. Shrink the cluster slowly within the NPH ensemble by smoothly and reversibly increasing the system's enthalpy $H_{\rm sys}$.

3. Above a threshold value for the system's enthalpy $H_{\rm sys} > H_{\rm SL}^{\rm th} < H_L^m$, where H_L^m is the liquid enthalpy at the melting point, the solid-liquid coexistence becomes unstable and solid-phase clusters shrink and vanish, eventually leaving a homogeneous liquid behind.

4. Store solid-liquid configurations along the shrinking trajectory. For each configuration, identify the cluster size $N_{\rm S}$ and the coexistence temperature $T_c(N_{\rm S})$. The latter is determined by switching to the NPT ensemble, and finding the temperature above which the cluster shrinks, and below which the cluster grows.

5. Find the smallest cluster size N_u, which grows to large sizes in the bcc phase without phase transformation. Smaller clusters of size $N_{\rm S} < N_u$ with coexistence temperatures $T_c(N_{\rm S}) < T_c(N_u) = T_u$, exhibit phase transformation to fcc/hcp when growing. In this way, we identify for every pressure P, the lower bound $T_u(P)$ to the kinetic stablility of bcc-phase clusters. Below this temperature, the growing bcc nuclei readily transform to close-packed structrues.

We have performed the above procedure for bcc-MSCL in 314928-particle computational cells and have extracted $T_u(P)$ at four pressures: 20, 30, 40, and 60 GPa. We have thus found that at large undercoolings, the growing bcc nuclei become structurally unstable towards phase transformation to the more stable close-packed phases. An illustrative example is shown in Fig. S9, which depicts a solid critical cluster at 30 GPa on the verge of dynamic instability. It was obtained by slowly shrinking a metastable bcc cluster in the NPH ensemble down to 200 particles with predominantly bcc symmetry. When growing this cluster at 1860 K in the NPT ensemble, it transitions to the fcc phase. However, at 1863 K, it grows to large sizes in the bcc phase. The conventional explaination for this instability is that the bulk bcc phase becomes dynamically unstable at sufficiently low temperatures (large undercoolings). As a contrast, we show below that fast interface kinetics can generate far-from-equilibrium nuclei outside the scope of CNT that can have reduced kinetic barriers towards solid-solid phase transformations. This mechanism is explicitly non-equilibrium and interface-driven and cannot be traced to the dynamical structural properties of the bulk crystal phase alone.

An example of such a transformation is shown in Fig. S10. An 800-particle mixed fcc/hcp-phase critical cluster, is obtained by shrinking a mixed fcc/hcp solid-liquid equilibrium, see Fig. 4(d), in the NPH ensemble at pressure $P = 70$ GPa. Growing this cluster by MD simulations in the NPT ensemble at the coexistence temperature $T_c = 2800$ K, causes partial transformation to the bcc phase shown in Fig. S10(a). Slightly larger critical clusters at coexistence temperatures above 2800 K do not exhibit structural transformation to bcc. It is hard to explain the partial transition to bcc, shown in Fig. S10(a), by energetic arguments purely based on the dynamical stability of the bulk bcc crystal. The reason for this is that the bcc phase is entropically stabilized at high temperatures with respect to the fcc phase, and therefore becomes only less stable as temperature is lowered. Hence, a mechanism involving explicit liquid-solid interface structure and dynamics must be invoked. We illustrate the role of interfacial kinetics in driving the structural phase transformation by simulating the growth of the same 800-atom cluster starting at the coexistence temperature $T_c = 2800$ K, but this time the growth rate is slowed down by continuous heating at a rate of 0.5 K/ps. The end result of this process is shown in Fig. S10(b), where it can be observed that the slower growth rate has suppressed transformation to bcc.

Extraneous-phase interface layers: Interfacial phase transformations and growth mode transitions

The mobilities of the (0001) interfaces in the linear mobility regime outside of the Δ_a temperature interval, were calculated using periodic slab geometries containing 160000 particles composed of $40 \times 20 \times 50$ hcp 4-atom orthorhombic unit cells. The mobilities of the $(11\bar{2}0)$ interfaces were calculated using periodic slab geometries containing 332800 particles composed of $52 \times 50 \times 32$ hcp 4-atom orthorhombic unit cells. All the studies involving the Δ_a temperature interval, the phase transformation and the growth mode transition were based on two-phase simulations in periodic slab geometries containing 640000 particles composed of $80 \times 40 \times 50$ 4-atom orthorhombic unit cells.

References

1. G.J. Martyna, D.J. Tobias, and M.L. Klein (1994) Constant Pressure Molecular Dynamics Algorithms. *J. Chem. Phys.* **101**(5):4177.
2. M. Parrinello, A. Rahman (1981) Polymorphic Transitions in Single Crystals: A New Molecular Dynamics Method. *J. Appl. Phys.* **52**(12):7182-7190.
3. M.E. Tuckerman, J. Alejandre, R. Lopez-Rendon, A.L. Jochim, G.J. Martyna (2006) A Liouville-Operator Derived Measure-Preserving Integrator for Molecular Dynamics Simulations in the Isothermal-Isobaric Ensemble. *J. Phys. A: Math Gen.* **39**(19):5629-5651.
4. W. Shinoda, M. Shiga, M. Mikami (2004) Rapid Estimation of Elastic Constants by Molecular Dynamics Simulation under Constant Stress. *Phys. Rev. B* **69**(13):134103.
5. L.A. Zepeda-Ruiz, B. Sadigh, A. A. Chernov, T. Haxhimali, A. Samanta, T. Oppelstrup, S. Hamel, L.X. Benedict, J.L. Belof (2017) Extraction of Effective Solid-Liquid Interfacial Free Energies for Full 3D Solid Crystallites from Equilibrium MD Simulations. *J. Chem. Phys.* **147**(19):194704.
6. P.R. ten Wolde, M.J. Ruiz-Montero, D. Frenkel (1995) Numerical Evidence for bcc Ordering at the Surface of a Critical fcc Nucleus. *Phys. Rev. Lett.* **75**(14):2714.
7. P.R. ten Wolde, M.J. Ruiz-Montero, D. Frenkel (1996) Numerical Calculation of the Rate of Crystal Nucleation in a Lennard-Jones System at Moderate Undercooling. *J. Chem. Phys.* **104**(24):9932-9947.
8. C. Desgranges and J. Delhommelle (2007) Controlling Polymorphism during the Crystallization of an Atomic Fluid. *Phys. Rev. Lett.* **98**(23):235502.
9. A. Samanta, J. Belof (2018) The Thermodynamics of a Liquid-Solid Interface at Extreme Conditions: A Model Close-Packed System up to 100 GPa. *J. Chem. Phys.* **149**(12):124703.

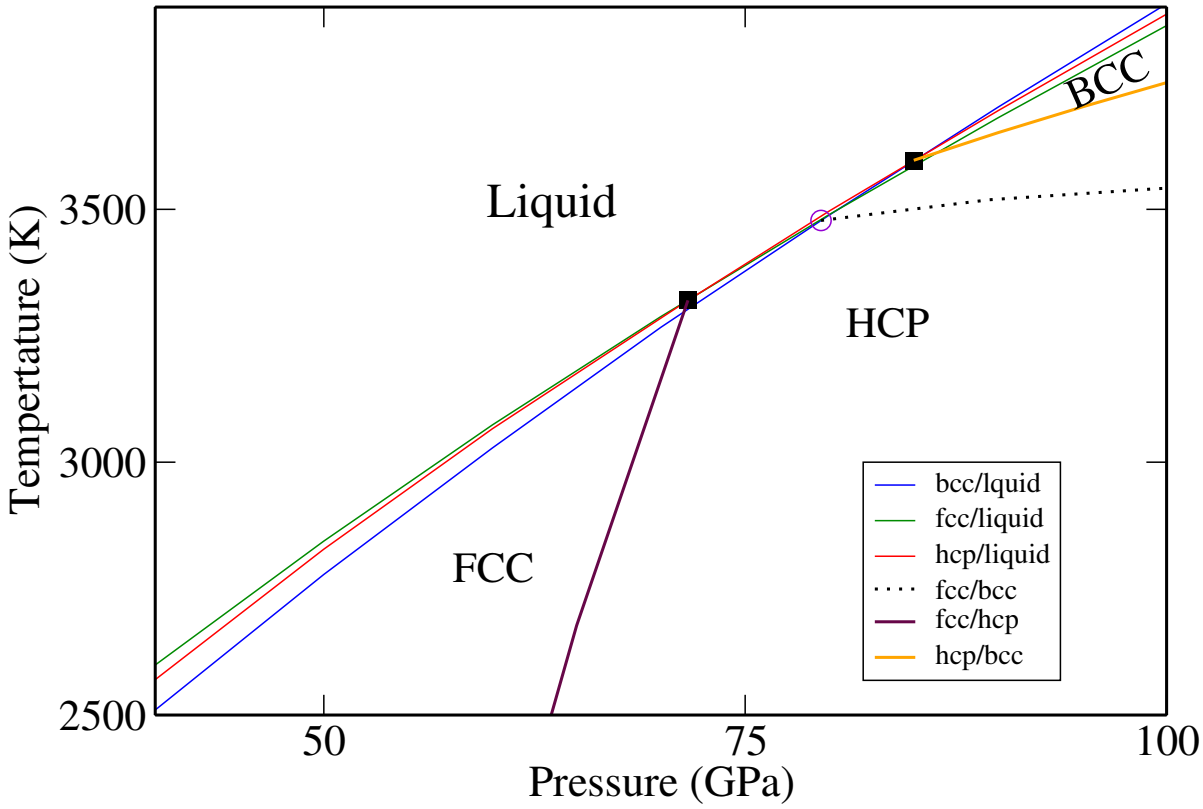

Fig. S1. Detailed temperature-pressure phase diagram of Mishin Cu model. There exist three bulk triple points: (i) liquid-hcp-fcc coexistence at 71.6 GPa and 3320 K, (ii) liquid-fcc-bcc coexistence at 79.5 GPa and 3478 K, and (iii) liquid-hcp-bcc coexistence at 85 GPa and 3598 K. The two thermodynamioc triple points at 71.6 GPa and 85 GPa are marked in the figure by two filled squares. The third triple point at 79.5 GPa is only metastable and is actually in the region of thermodynamic stability of the hcp phase. It is marked in the figure by the open circle.

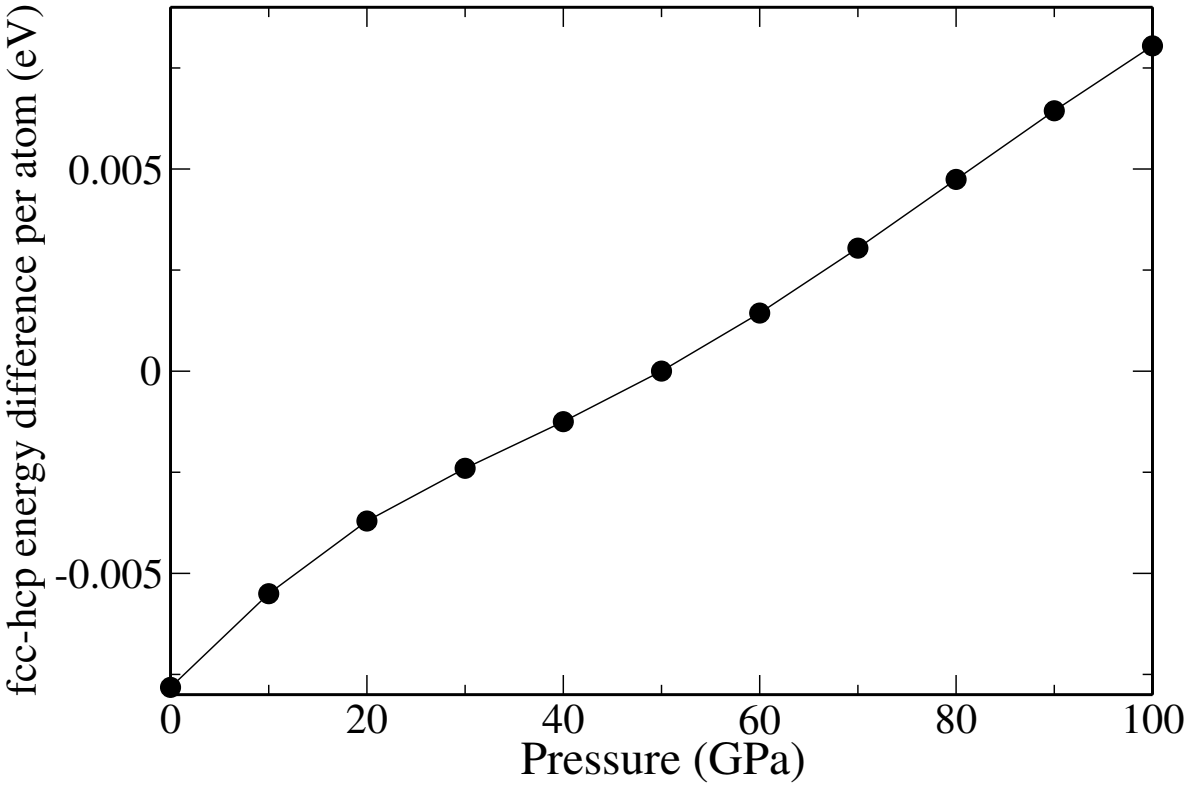

Fig. S2. Energy difference between the fcc and the hcp phases as a function of pressure at 0 K. Note the transition pressure at 50 GPa. Below this pressure fcc is the stable phase, and above it, hcp becomes stable.

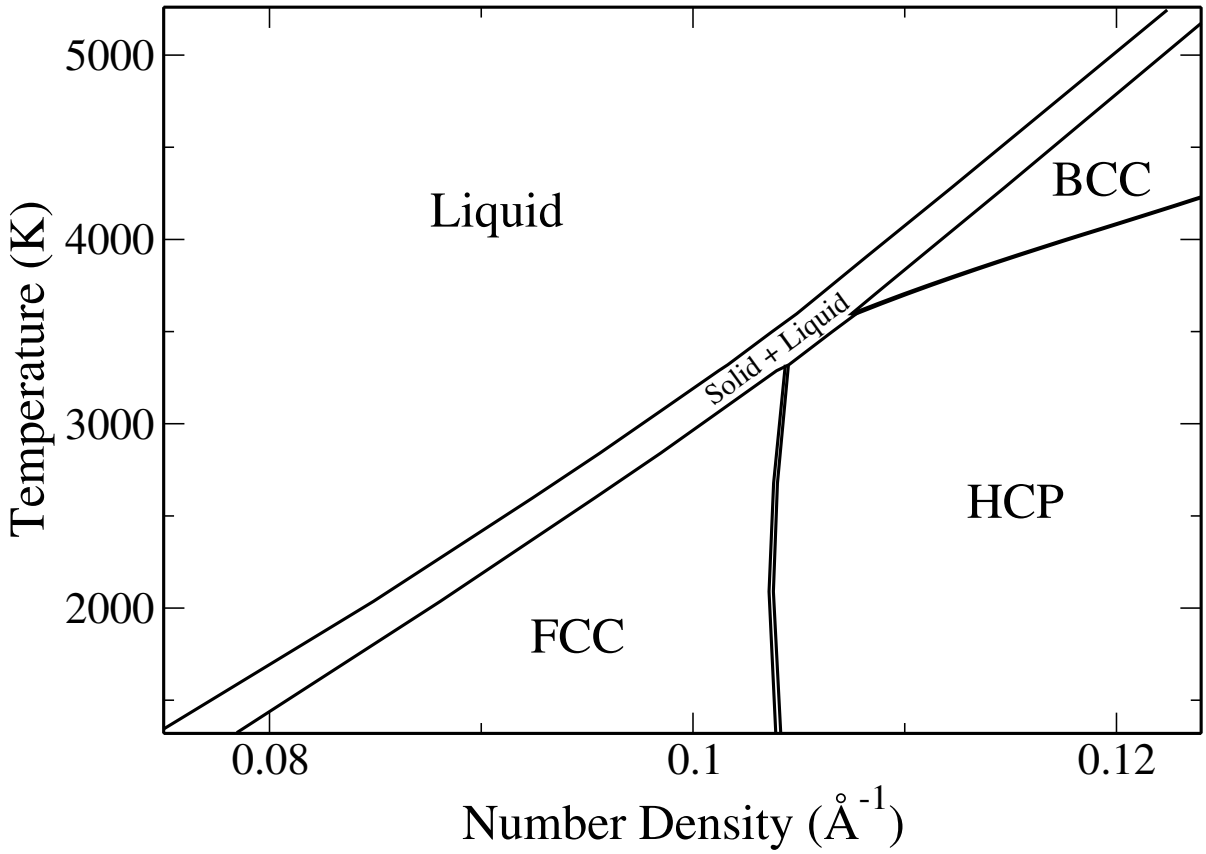

Fig. S3. Thermodynamic phase diagram of the EAM-Cu model in the temperature-density plane. Its representation in the temperature-pressure plane is depicted in Fig. 1 of the main text.

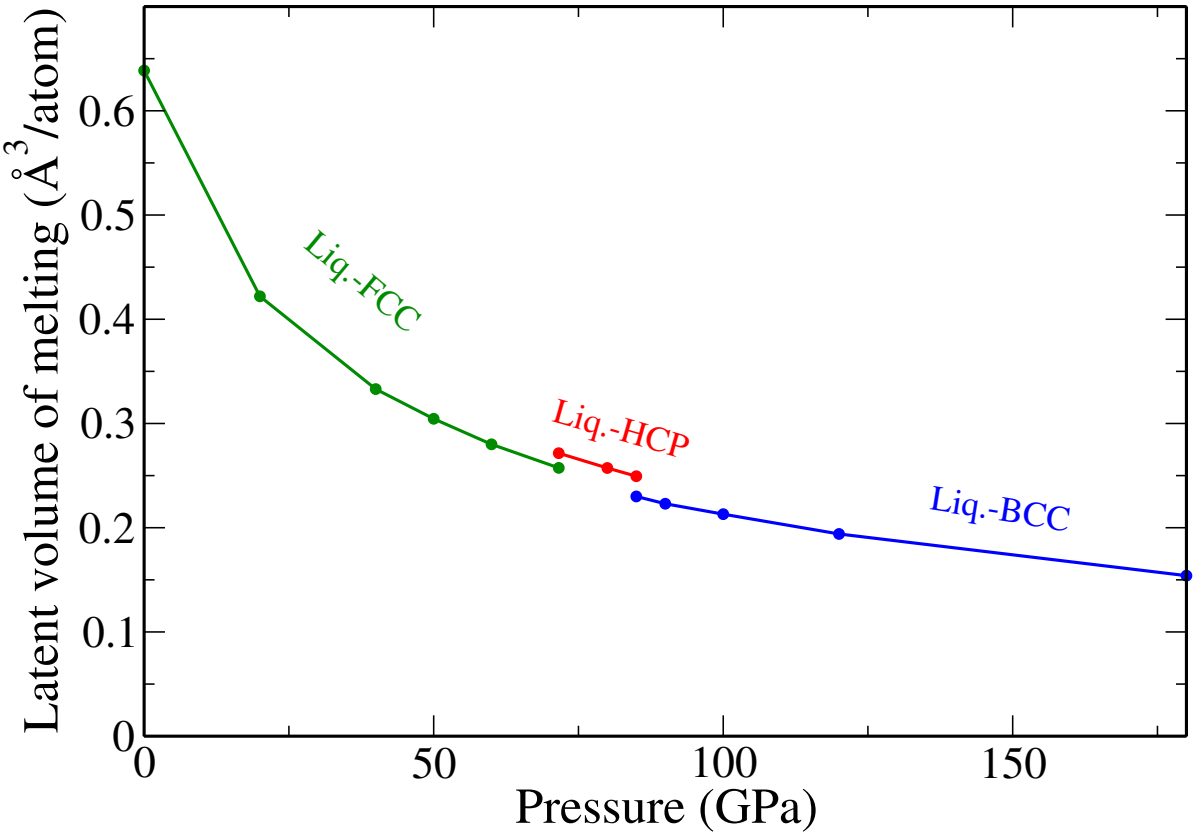

Fig. S4. Latent volumes of melting (the difference in volume between the liquid and the solid phases at coexistence) as a function of pressure. The different colors depict the different solid phases (fcc:green, hcp: red, bcc: blue), from which equilibrium melting occurs.

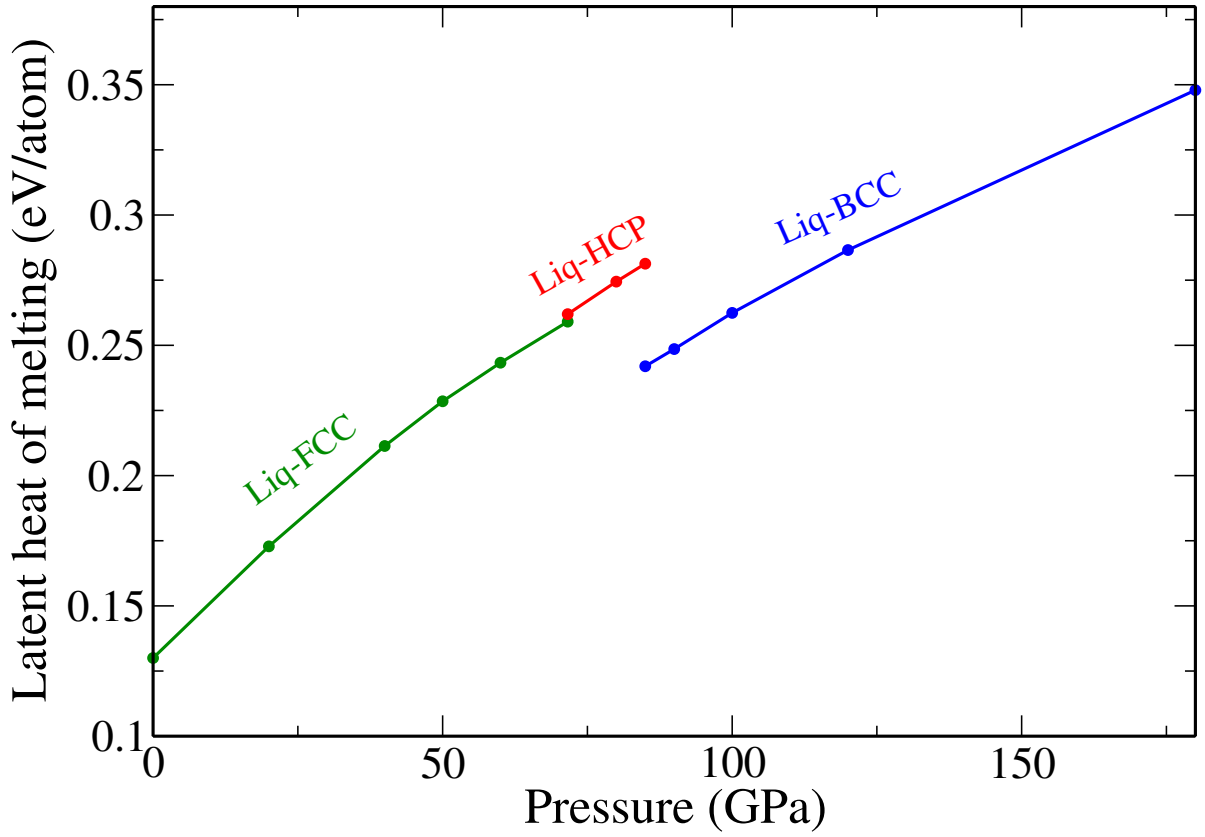

Fig. S5. Latent heats of melting (the difference in enthalpy between the liquid and the solid phases at coexistence) as a function of pressure. The different colors depict the different solid phases (fcc:green, hcp: red, bcc: blue), from which equilibrium melting occurs.

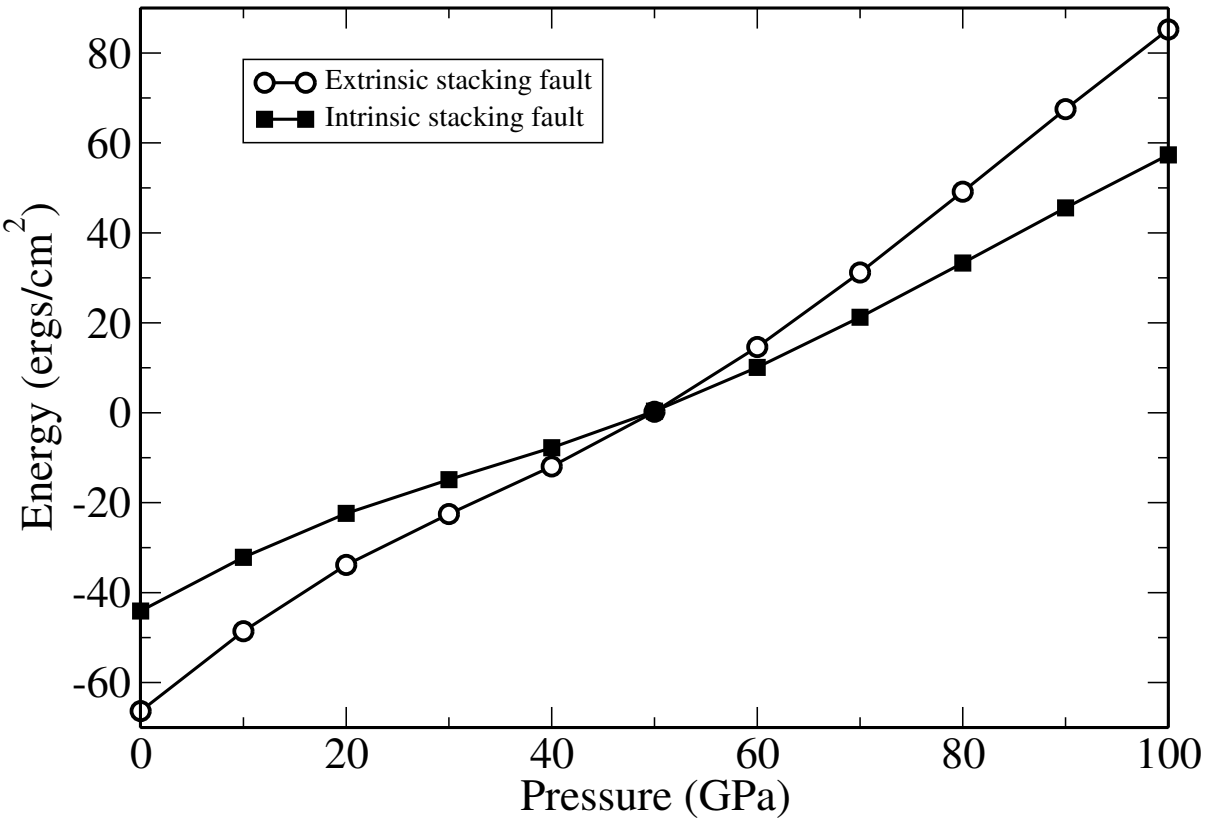

Fig. S6. The energies of an extrinsic and an intrinsic stacking fault in the hcp phase at 0 K. The negative energies at small pressures reflect the stability of the fcc phase.

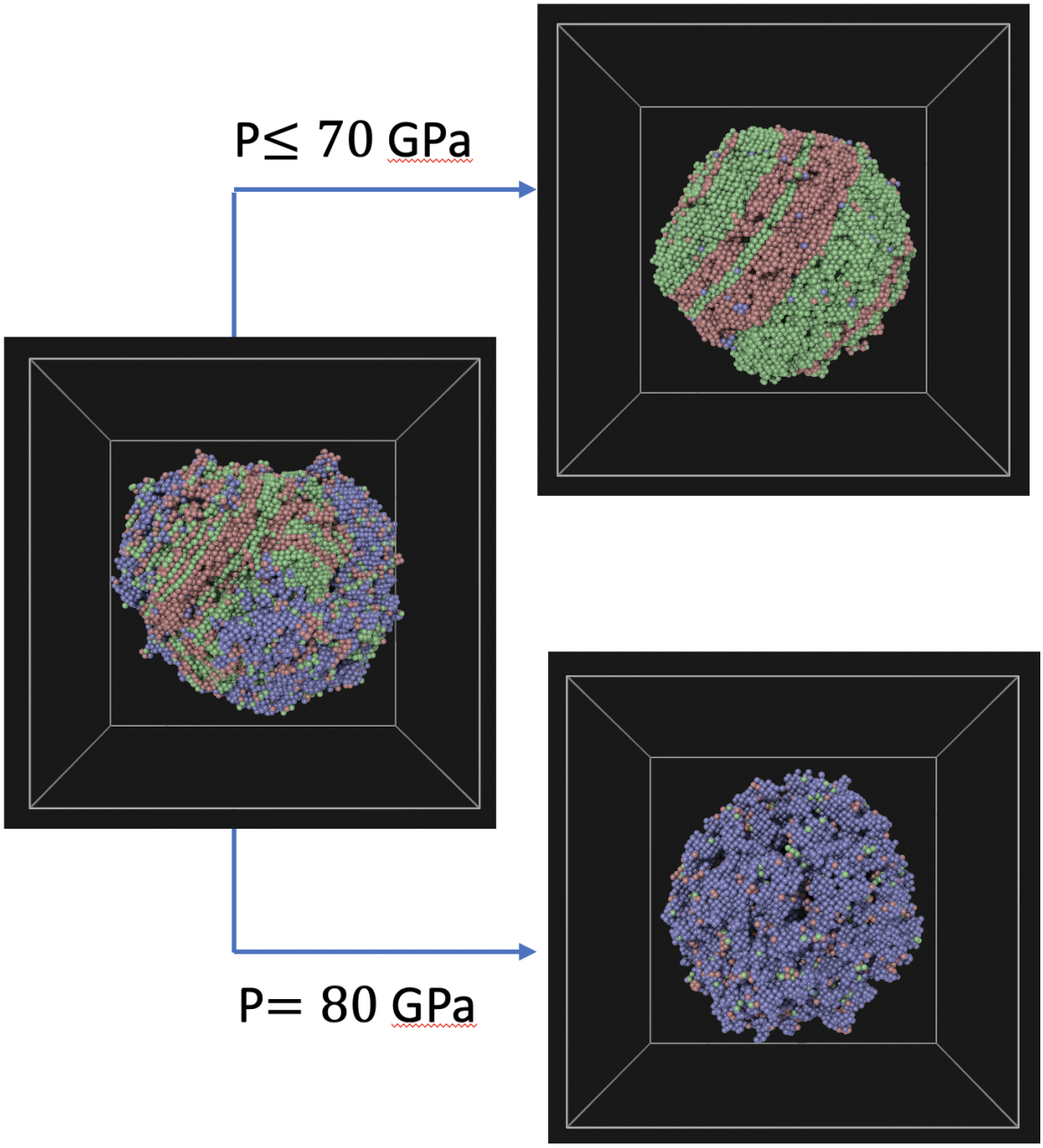

Fig. S7. A mixed bcc-fcc-hcp cluster embedded in liquid obtained from an unstable postcritical bcc cluster at 60 GPa and 2200 K. Upon equilibration in the NPH ensemble, it relaxes into the mixed fcc/hcp metastable-cluster configuration at pressures 70 GPa and below. At 80 GPa it can equilibrate to a bcc cluster configuration in coexistence with the melt.

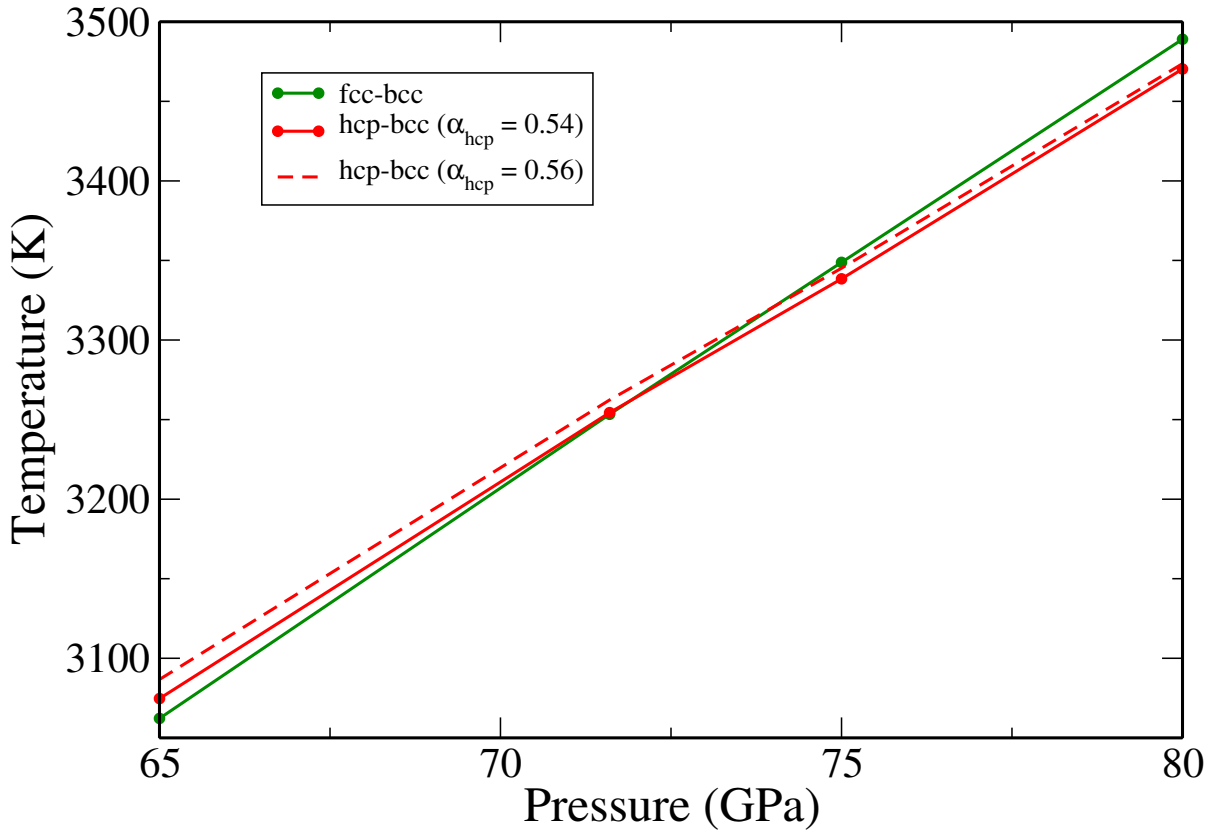

Fig. S8. Solid-nucleation phase boundaries. The solid lines depict $T^*_{\text{fcc}}(P)$ (green) and $T^*_{\text{hcp}}(P)$ (red), assuming $\alpha_{\text{fcc}} = \alpha_{\text{hcp}} = 0.54$. The dashed line shows $T^*_{\text{hcp}}(P)$ for $\alpha_{\text{hcp}} = 0.56$.

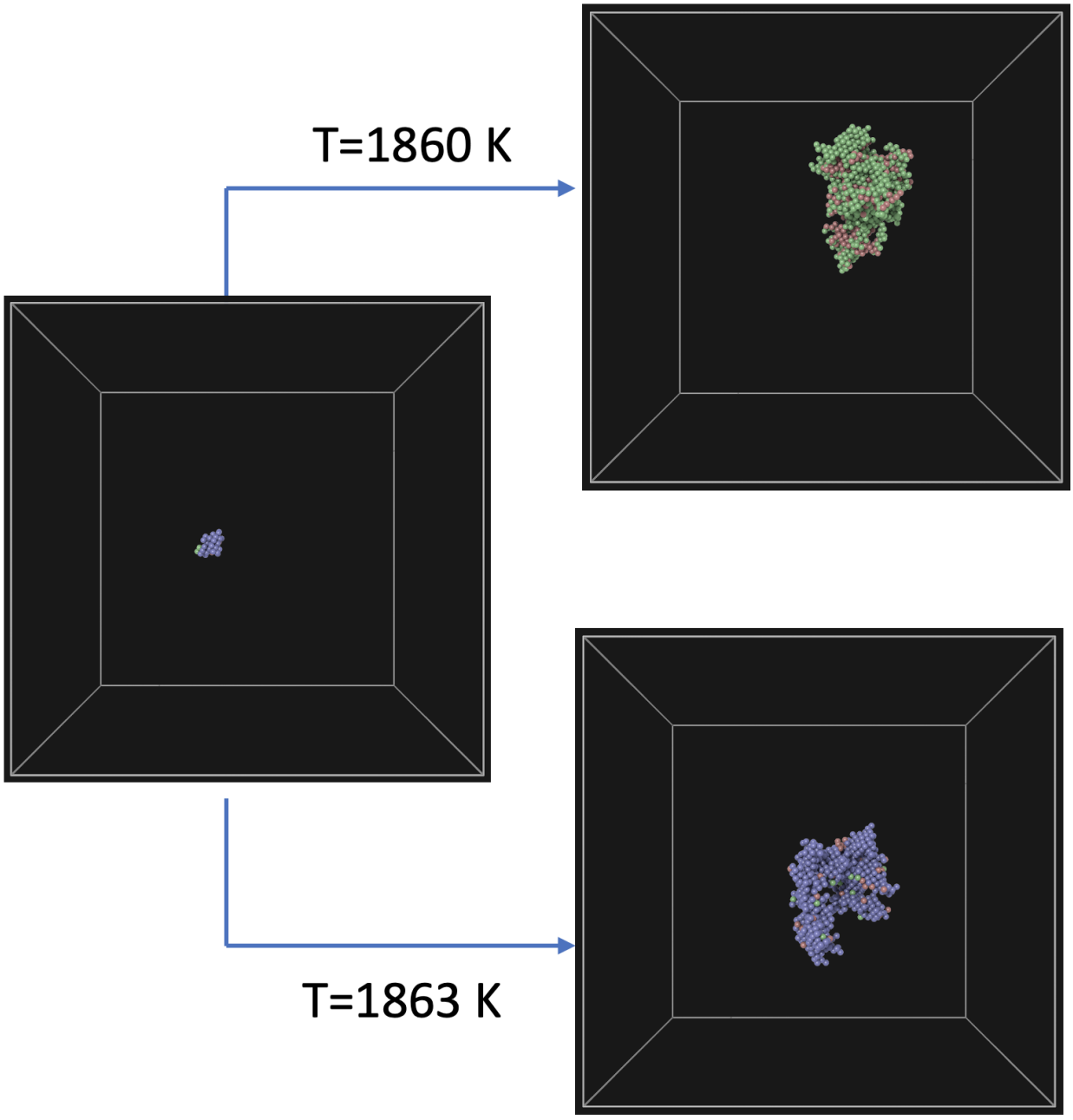

Fig. S9. Example of a bcc critical cluster on the verge of kinetic phase stability. A 200-particle cluster is obtained by continuous shrinking of a metastable bcc cluster, see Fig. 3(b) in the main text, at 30 GPa, via reduction of the total enthalpy of the system in an NPH ensemble. The results of two NPT simulations at 1860 K and at 1863 K is shown. At 1860, the growing cluster transforms to fcc, while at 1863 K, no phase transformation is observed. Particles with bcc symmetry are shown in blue, fcc symmetry in green, and hcp symmetry in red.

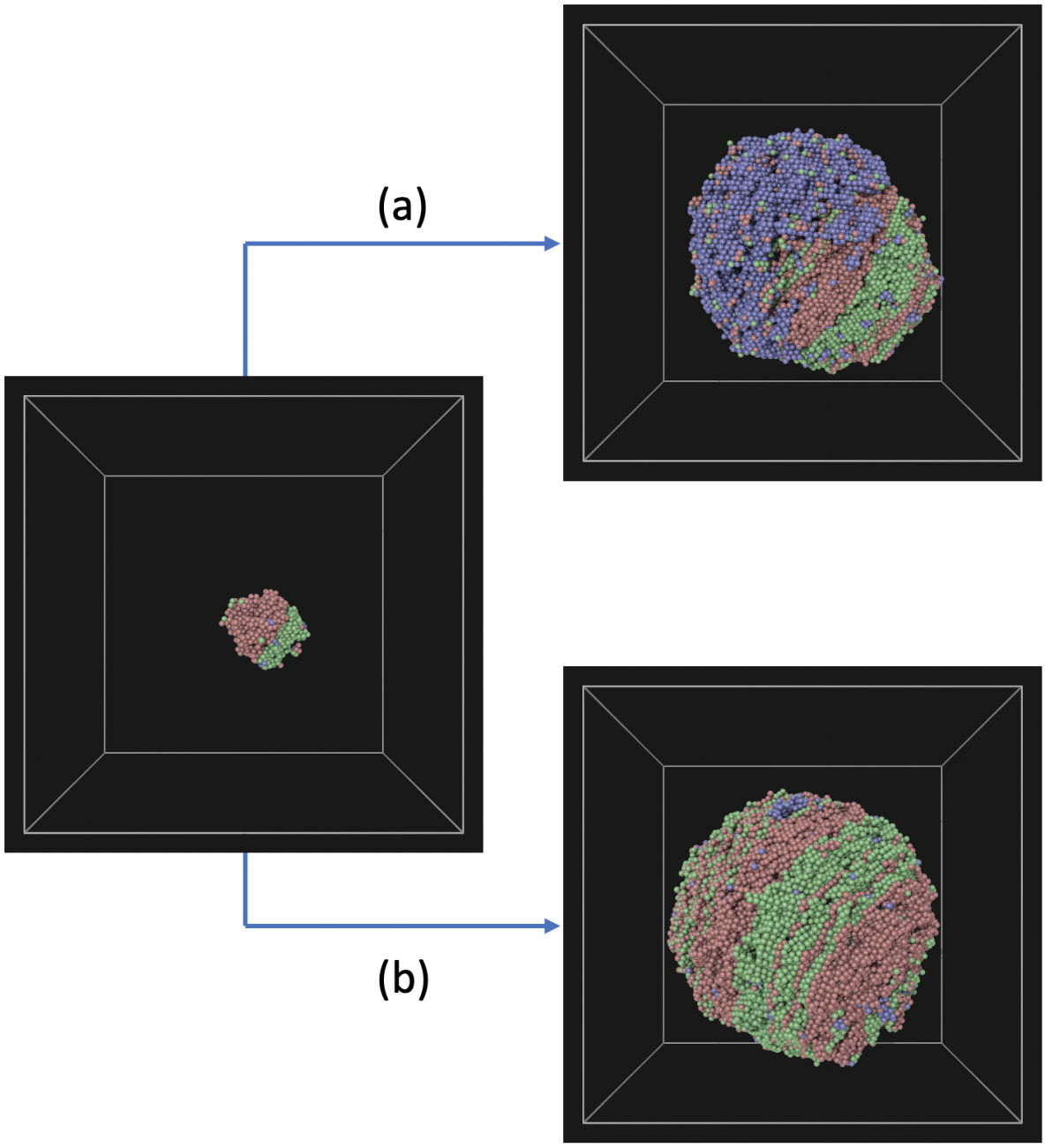

Fig. S10. Example of a far-from-equilibrium solid-cluster-phase evolution. An 800-particle cluster is obtained by continuous shrinking of a mixed fcc/hcp cluster, see Fig. 3(d) in the main text, at 70 GPa, via reduction of the total enthalpy of the system in an NPH ensemble. This cluster shrinks and disappears in NPT ensembles at temperatures above 2800 K. Two simulations of cluster growth are shown: (a) Fast growth NPT simulation at 2800 K, and (b) Slow growth NPT simulation starting at 2800 K, and continuously heated at a rate of 0.5 K/ps. Subsequent annealing of the outcomes of both simulations in an NPH ensemble produces the equilibrium embedded fcc/hcp mixed-phase cluster, shown in Fig. 3(d) in the main text. Particles with bcc symmetry are shown in blue, fcc symmetry in green, and hcp symmetry in red.

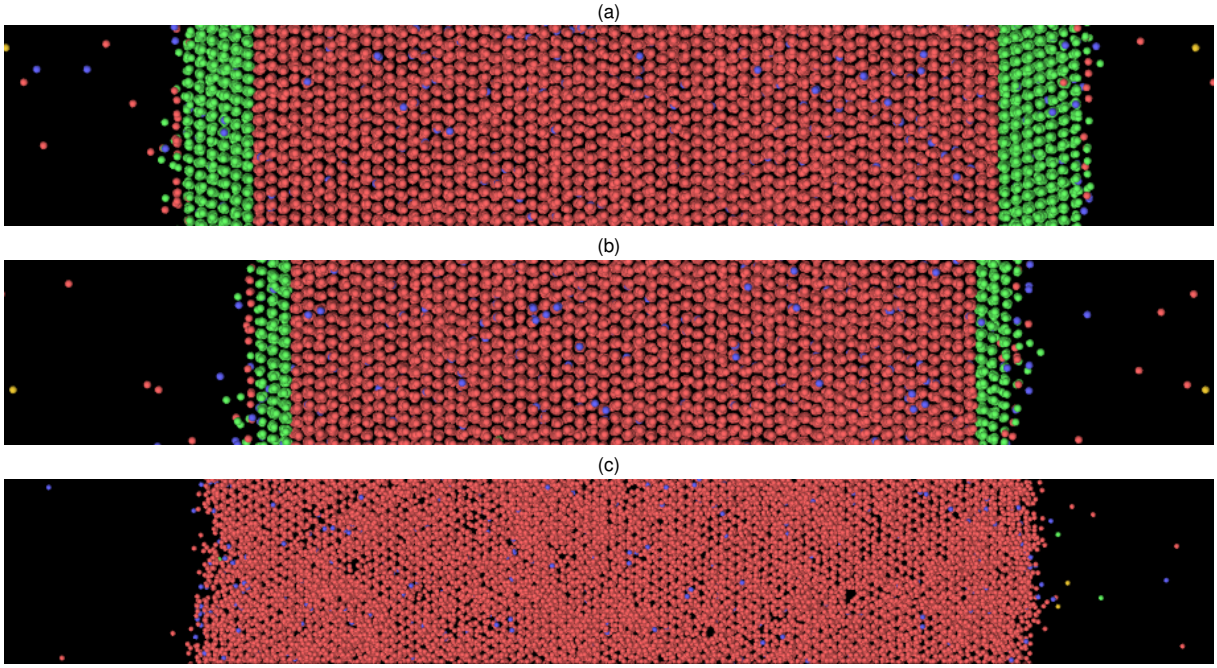

Fig. S11. Side views of liquid-solid slab equilibria at 80 GPa. The bulk crystal phase (red particles) is hcp and the green particles represent occurrence of fcc symmetry mainly at the interface with the liquid. The particle symmetries are classified via adaptive cutoff common-neighbor analysis, and the non-crystalline particles have been deleted. (a) and (b) depict hcp-(0001) interfaces with the liquid. At the liquid interface, the solid transforms to fcc domains with fcc-(111) planes parallel to the interface. The two-phase equilibrium temperatures are (a) 3492 K, and (b) 3500 K. (c) depicts hcp-$(11\bar{2}0)$ interfaces with the liquid at a temperature of 3497 K.

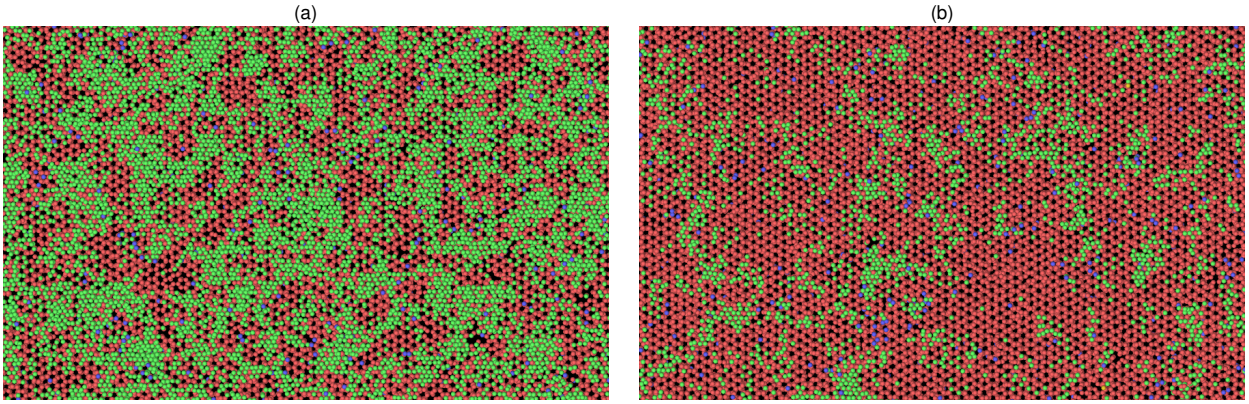

Fig. S12. Top view cross sections of the solid liquid-solid equilibria shown in Fig. S11(a) and (b). The bulk crystal phase (red particles) is hcp and the green particles represent occurrence of fcc symmetry right at the interface. The particle symmetries are classified via adaptive cutoff common-neighbor analysis, and the non-crystalline particles have been deleted.

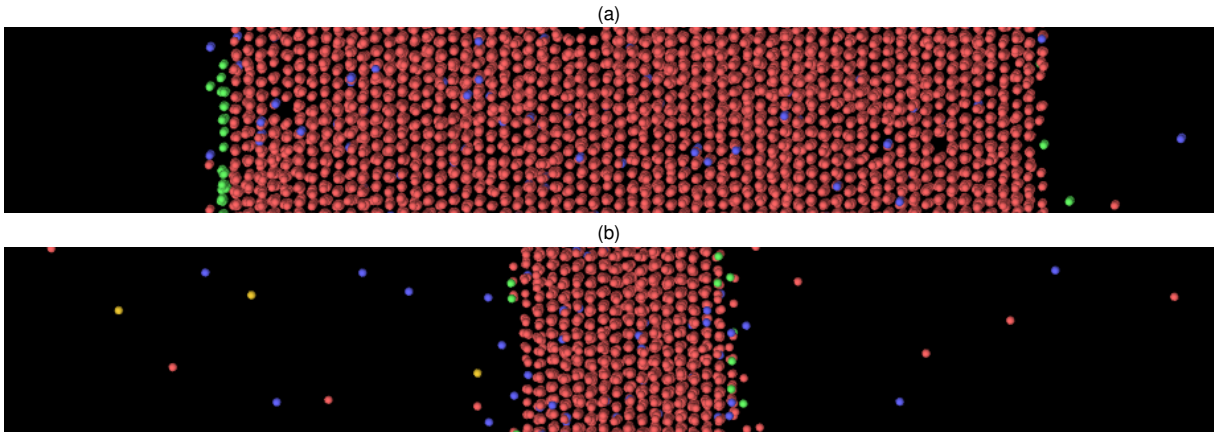

Fig. S13. Side view of two snap shots of a solid-liquid system at 80 GPa with the solid phase shrinking due to superheating at 3520 K. (a) initial configuration, and (b) configuration at about 1 ns later. The particles are classified via adaptive cutoff common-neighbor analysis, with the hcp particles colored red, fcc particles green, and bcc particles blue, The non-crystalline particles have been deleted.

(a)

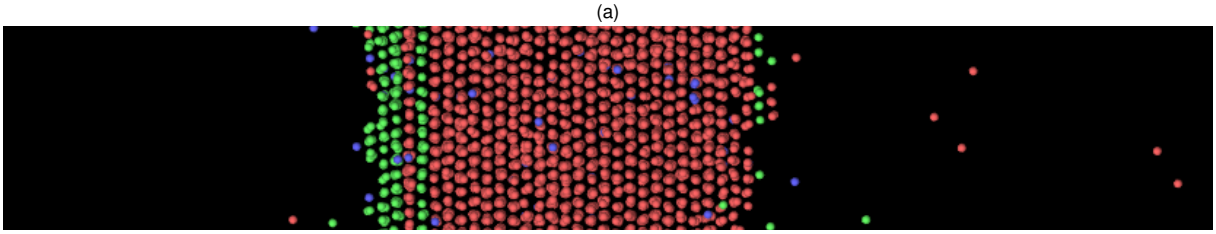

(b)

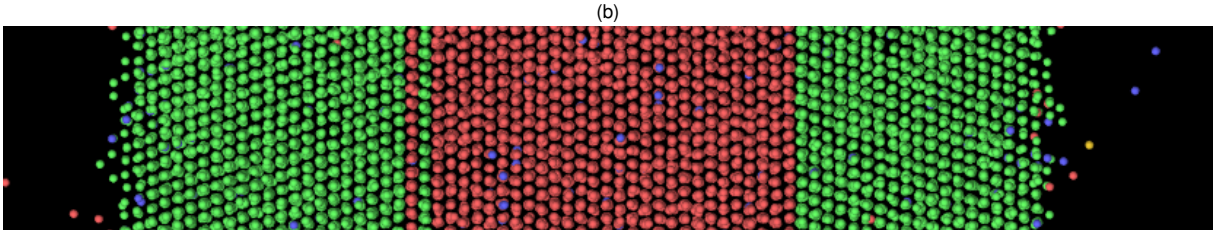

Fig. S14. Side view of two snap shots of a solid-liquid system at 80 GPa with the solid phase growing due to undercooling at 3480 K. (a) initial configuration, and (b) configuration at about 3 ns later. The particles are classified via adaptive cutoff common-neighbor analysis, with the hcp particles colored red, fcc particles green, and bcc particles blue, The non-crystalline particles have been deleted. The close-packed stacking sequence is ..BACBACABAB.. at the left interface and ..ABABCABCAB... at the right one, resulting in the twin relation between the left and the right fcc films.

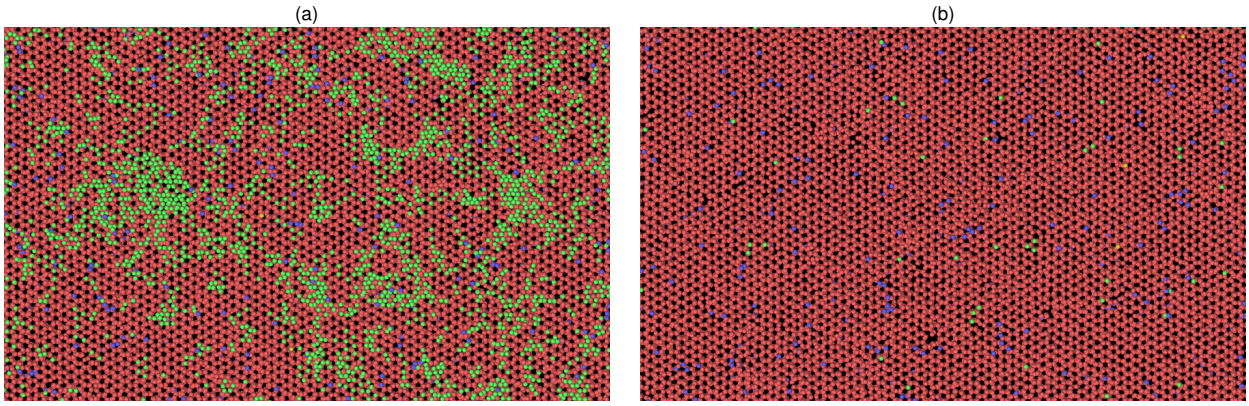

Fig. S15. Top view of cross sections of two snap shots of the NPT-MD simulation at $P = 80$ GPa, and $T = 3503$ K, shown in Fig 8(b) of the main text. The bulk crystal phase (red particles) is hcp and the solid-liquid interface plane is hcp-(0001). The interface contains fcc domains (green particles) with fcc-(111) planes parallel to the interface. The particles are classified via adaptive cutoff common-neighbor analysis, and the non-crystalline particles have been deleted. The two snap shots are (a) initial configuration at time ($t = 0$) in phase II, and (b) the configuration at time ($t = 9.5$ ns) in phase I.